Eidgenössische Technische Hochschule Zürich
Swiss Federal Institute of Technology Zurich

Study of SMEFT BSM operators in the context of the CMS $H \to \gamma\gamma$ analysis using NLO simulation

Master Thesis in Physics

Bardh Quni

September, 2020

CERN-THESIS-2020-109
15 October 2020

Supervisor: Prof. Dr. Günther Dissertori

Department of Physics, Institute for Particle Physics and Astrophysics (IPA), ETH Zürich

Abstract

We consider the Higgs boson differential production cross-sections for gluon fusion as a function of several observables. Being a loop induced process, gluon fusion can be used to indirectly search for New Physics (NP) beyond the Standard Model (SM). In particular, we study the impact of introducing dimension-six operators on the differential production cross-sections. The study is performed in the framework of the Standard Model Effective Field Theory (SMEFT) at Next to Leading Order (NLO) QCD, using MADGRAPH5_AMC@NLO framework.

Acknowledgements

First and foremost, I thank Prof.Günther Dissertori for allowing me to work on this project based at CERN and supporting me through the entire process. A big thank also goes to Simone Pigazzini for always having an open door and answering all my questions, be it physics or software. I want to thank Mauro Donega for being a great coordinator of the project, and for the excellent collaboration both on the technical and the physics side. Last but not least, I thank all researchers at CERN that were part of the ETH group for being a lovely company in lunch breaks and every other occasion.

Contents

Chapter 1

Introduction

The standard model is a very elegant and simple theory that describes the fundamental interactions between elementary particles. In mathematical language, the Standard Model is a Quantum Field Theory which is symmetric upon non-abelian gauge group $SU(3)_C \otimes SU(2)_L \otimes U(1)_Y$. The first part or $SU(3)_C$ symmetry describes the interaction between quarks and gluons which is known as QCD. While the second part $SU(2)_L \otimes U(1)_Y$ describes the electroweak theory [41]. The framework of SM is based on the spontaneously broken electroweak symmetry which leads to massive particles and the scalar resonance which we know as Higgs particle. Thanks to direct searches at the Large Hadron Collider (LHC) we were able to find this new resonance. The LHC, a 26.7 km diameter superconducting proton-proton collider is the largest particle accelerator ever built, which generates the collision at centre of mass-energy in the 7-14 TeV range [21]. The discovery of Higgs boson as the 125 GeV scalar resonance by the ATLAS and CMS experiments at LHC was a triumph for the Standard Model because within the present statistical precision is compatible with the predictions of the model [17][18]. Despite the success of the SM, it does not address some of the unsolved problems in physics such as baryon asymmetry of the Universe[45], evidence for dark matter[20, 40, 12] or neutrino masses[6, 38, 43, 35, 36]. Theories that try to solve the problems mentioned above include various extensions of the SM through supersymmetry (SUSY), such as Minimal Supersymmetric Standard Model (MSSM), string theory or extra dimension. The search for New Physics (NP) always proceeds by following two approaches: direct searches or new states and indirect searches through deviations from the predictions. A way to systematize possible deviations from the SM is to use Standard Model Effective Field Theory (SMEFT) which is a consistent field theory to characterize the low energy limit of physics beyond the SM [7]. New resonances that may exist at the energy scales beyond the reach of LHC are effectively decoupled from the SM, allowing to freeze those extra degrees of freedom. New Physics could manifest by small deviations from the SM predictions which one can check in [29]. To consistently introduce the deviations from the Standard Model (SM) we treat the SM as an effective field theory, therefore, we use the bottom-up framework known as Standard Model Effective Field Theory (SMEFT). In this approach, we extend the SM Lagrangian by augmenting it with the class of operators which are relevant for the processes we want to investigate. Since our work is concentrated in Higgs Physics we work with dimension-six operators which are suppressed by a New Physics scale Λ. Then we move on the phenomenological impact that variations of the Wilson coefficients have on the NLO cross-section shape of the observable which we obtain with *MADGRAPH5_AMC@NLO*. The goal of this master thesis is to consider the phenomenological impact of the NLO corrections coming from these operators by using MADGARPH5_AMC@NLO . Kinematical distributions provide an important handle on the determination of the Higgs properties. Among the most sensitive observables is Higgs transverse-momentum distribution. The transverse momentum spectrum deformations provide more information than the total cross-section and allow us to disentangle effects that remain hidden in the total rates.

At the LHC there are different Higgs-production channels. The LO Feynman diagrams for the four different production channels for a single Higgs boson at hadron collider are shown in Figure 1.1 to 1.4 [4]. The Higgs-production channel with the largest cross-section at the LHC is the gluon fusion, which despite being a loop-induced process is enhanced by the gluon parton density function of the proton [31]. For the gluon fusion process of single Higgs production the QCD corrections are known up to N^3LO in the limit of the heavy top quarks[2, 13, 14, 23, 9, 44, 10] while for the case of full quark-mass dependence is only known up to NLO [16, 15, 39, 11].The main decay channel (see Fig.2.2) that we deal in this work is the diphoton final state which also served as one of the key discovery channels for the Higgs. The reason behind choosing this decay channel is because it is a very clean experimental channel, due to the excellent energy resolution of the calorimeter in the LHC experiments, and is the one providing the largest statistical power. Besides, it is also well suited for precision studies of the Standard Model (SM) and in particular the Higgs sector [28].

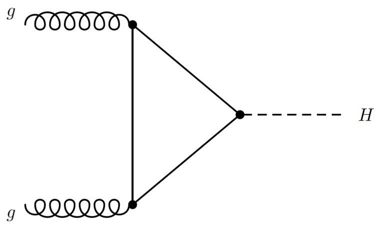

Figure 1.1: Gluon fusion

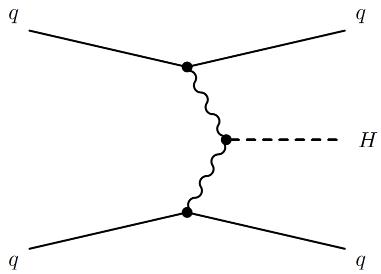

Figure 1.2: Vector-Boson fusion

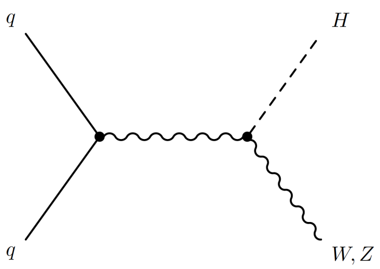

Figure 1.3: Higgs strahlung

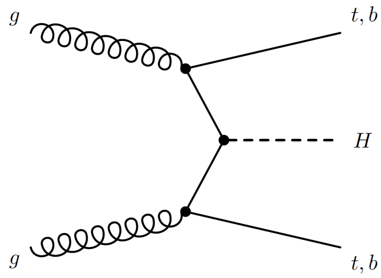

Figure 1.4: Higgs bremsstrahlung off top-quarks

The thesis is organized as follows. In section 2 we introduce the SMEFT framework as a tool to probe new physics in the low energy limit by presenting dimension-six operators and moving forward to SMEFT at NLO. In section 3 we present our phenomenological results based on the modification of the LO cross-section including dimension-six operators for the observables. In section 4 we summarize our results and provide some concluding remarks.

Chapter 2

SMEFT framework

In this section, we introduce the SMEFT framework. After that, we present some of the dimension-six operators stressing the operators which are relevant for the Higgs production and decay processes, using the analytical expressions for single Higgs boson production and decay width at LO in the SMEFT.

2.1 Introduction to SMEFT

The SMEFT is a consistent EFT extension of the SM built out of SM fields. The idea of the SMEFT is that of deformation of the SM without including new low energy particles. We consider the effective Lagrangian of the form

$$\mathcal{L}_{SMEFT} = \mathcal{L}_{SM} + \mathcal{L}^5 + \mathcal{L}^6 + , \ldots, \quad \text{where} \quad \mathcal{L}^d = \sum_{i=1}^{n_d} \frac{C_i^d}{\Lambda^{d-4}} \mathcal{Q}_i^d \tag{2.1}$$

The operators $\mathcal{Q}_i^d$are suppressed by d-4 powers of the cutoff scale Λ and the $\mathcal{C}_i^d$ are the Wilson coefficients which are dimensionless. The dimensionless of the Wilson coefficient or the fact that the operators are suppressed by Λ^{d-4} will help in theoretical aspect when studying the Re-normalization Group Equation (RGE) to study the evolution of these coefficients from a UV scale down to an electroweak scale where the dimension-six operators are relevant for Higgs processes. In the SM these coefficients are zero. Therefore any deviations from zero is an indication of the new physics in the corresponding effective interaction vertex. One problem with the SMEFT is that it has a huge amount of operators. Without any assumptions on the operator structure, we have 2499 parameters or better to say the Warsaw basis closes at one loop and the full 2499 x 2499 anomalous dimension matrix is determined[7]. The Warsaw basis[5] is a non-redundant operator basis for $\mathcal{L}^6$ which took twenty-four years after Ref.[46] was published. The non-redundant basis it is built upon field redefinition of the SM fields $\mathcal{O}\left(\frac{1}{\Lambda^2}\right)$ by removing the combination of $\mathcal{L}^6$ operators such that they vanish in the Lagrangian before the S matrix element is constructed. The removal of redundant operator it is done in gauge independent manner because observables (i.e. S matrix elements) are invariant under gauge independent field redefinitions[7]. Yet, without assumptions , we get n_d = 2499 operators. One of the assumptions that we are using is that coefficients of D=6 operators are flavour universal which brings the number of independent parameters down to 76. Furthermore, only 9 of them will be relevant for the general description of the Higgs signal strength measurements [19]

2.2 SMEFT Operators

The $\mathcal{L}^6$ operators built from the Standard Model fields which conserve baryon number in the Warsaw basis are fully presented in[5]. Following [33] we will present just some of the dimension-six operators that create this basis.

2.2.1 Dimension 6,X^3

There are 2 CP-even and 2 CP-odd operators with three field strength tensors.

X^3
Q_G=$f^{ABC}G_\mu^{A\nu}G_\nu^{B\rho}G_\rho^{C\mu}$
$Q_{\tilde{G}}$=$f^{ABC}\tilde{G}_\mu^{A\nu}G_\nu^{B\rho}G_\rho^{C\mu}$
Q_W=$\varepsilon^{IJK}W_\mu^{I\nu}W_\nu^{J\rho}W_\rho^{K\mu}$
$Q_{\tilde{W}}$=$\varepsilon^{IJK}\tilde{W}_\mu^{I\nu}W_\nu^{J\rho}W_\rho^{K\mu}$

2.2.2 Dimension 6,H^6

There is a single CP-even operator involving six Higgs fields. It adds a h^6 interaction of the physical Higgs particle to the SMEFT Lagrangian after spontaneous symmetry breaking.

H^6
$Q_H = (H^\dagger H)^3$

2.2.3 Dimension 6,H^4D^2

The H^4D^2 operators are self-interactions of the Higgs doublets as quartic interactions with additional derivatives and impact the self-interactions of the Higgs boson.

H^4D^2
$Q_{H\Box} = (H^\dagger H)\Box(H^\dagger H)$
$Q_{HD} = (H^\dagger D_\mu H)^*(H^\dagger D_\mu H)$

2.2.4 Dimension 6,X^2H^2

The X^2H^2 operators are very important phenomenologically. They lead to $gg \to H$ and $H \to \gamma\gamma$ vertices and contribute to Higgs production and decay, something which is relevant for us because we deal with this sector in this work. The corresponding SM amplitudes start at one loop, so LHC experiments are sensitive to X^2H^2 operators via interference effects with SM amplitudes[22, 32]

X^2H^2
$Q_{HG} = H^\dagger H G^A_{\mu\nu} G^{A\mu\nu}$
$Q_{H\tilde{G}} = H^\dagger H \tilde{G}^A_{\mu\nu} G^{A\mu\nu}$
$Q_{HW} = H^\dagger H W^I_{\mu\nu} W^{I\mu\nu}$
$Q_{H\tilde{W}} = H^\dagger H^I \tilde{W}^I_{\mu\nu} W^{I\mu\nu}$
$Q_{HB} = H^\dagger H B_{\mu\nu} B^{\mu\nu}$
$Q_{H\tilde{B}} = H^\dagger H \tilde{B}_{\mu\nu} B^{\mu\nu}$
$Q_{HWB} = H^\dagger \tau^I H W^I_{\mu\nu} B^{\mu\nu}$
$Q_{H\tilde{W}B} = H^\dagger \tau^I H \tilde{W}^I_{\mu\nu} B^{\mu\nu}$

2.2.5 Dimension 6, ψ^2H^3

These operators are $(H^\dagger H)$ times the SM Yukawa couplings, and they violate the relation that the Higgs boson coupling to fermions is proportional to their mass[33].

ψ^2H^3
$Q_{eH} = (H^\dagger H)(\bar{l}_p e_r H)$
$Q_{uH} = (H^\dagger H)(\bar{q}_p u_r H)$
$Q_{dH} = (H^\dagger H)(\bar{q}_p d_r H)$

There are of course operators of dimension 5 which are assumed to be generated at very high energy scale and give a Majorana neutrino mass but they are not relevant for Higgs processes but neutrino physics. As mentioned at the beginning of this section the full table of operators you can check on [5].

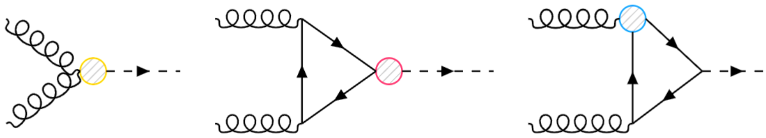

Figure 2.1: Feynman diagrams to LO process for $\mathbf{gg} \to \mathbf{H}$.The possible insertion of the EFT operators is indicated with colored blobs.Contribution from $\mathcal{O}_1$(orange) , $\mathcal{O}_2$(purple), $\mathcal{O}_3$(blue)

In this master thesis, our main focus for the impact on observables will be on the following operators:

$$\mathcal{O}_1 = |H|^2 G^a_{\mu\nu} G^{a,\mu\nu} \tag{2.2}$$

$$\mathcal{O}_2 = |H|^2 \bar{Q}_L H^c t_R + h.c. \tag{2.3}$$

$$\mathcal{O}_3 = \bar{Q}_L H \sigma^{\mu\nu} T^a t_R G^a{}_{\mu\nu} + h.c. \tag{2.4}$$

$$\mathcal{O}_4 = |H|^2 B_{\mu\nu} B^{\mu\nu} \tag{2.5}$$

The operator $\mathcal{O}_1$ is a CP conserving operator which corresponds to direct coupling of the Higgs with gluons something which is not present in SM. The tree-level contribution in the SM is mediated by heavy quarks, like top quark. The operator $\mathcal{O}_2$ describe the modification of the top Yukawa couplings. The operator $\mathcal{O}_3$ is the chromomagnetic dipole-moment operator, which modifies the interaction between the gluons and the top quark. Possible insertion of these dimension-six operators can be seen in Figure2.1. For the operator $\mathcal{O}_3$ there has been studied, where also the analytical results are obtained in[30]. The operator $\mathcal{O}_4$ is CP conserving operator contributing to Higgs decay (see Fig.2.2) mediated by heavy gauge boson and top loop [24].

2.3 Higgs production and decay in the SMEFT

Following [7], we express the partonic cross-section for single Higgs production and the partial width computed at tree level in the SMEFT. As we mentioned in the introduction the dominant Higgs production channel at the LHC is gluon fusion which is a loop induced process. The leading contribution comes from top quark, whereas in heavy quark EFT we also have contact interaction between the Higgs and gluons $HG^a_{\mu\nu}G^{\mu\nu}_a$, this coupling receives a contribution from the $\mathcal{O}_1$ and leads to the modification of the Higgs production[32]. Also, since we will use SMEFT at NLO we will need to know NLO contributions from $\mathcal{O}_1$. Therefore, we know NLO contributions from $\mathcal{O}_1$ because they are the same to the NLO corrections to gluon-fusion in the SM where the top quark is infinitely heavy [13]. The leading SM contribution(at tree-level in the EFT obtained in the infinitely heavy top quark) gives the partonic cross section[13, 2]

$$\sigma^{SM}(gg \to H) = \frac{G_F \alpha_s^2}{32\sqrt{2}\pi} |I^g|^2 \tag{2.6}$$

where $|I^g|^2$ is a Feynman integral that accounts for the top-quark loop contribution. The value of this integral is $1/3$ when the QCD corrections are omitted and when we deal with limit $\frac{m_h}{m_t} \to 0$. Including the QCD corrections up to NLO, the integral takes different form [32, 13, 2]. The standard model amplitude is dominated by integrating out the top quark

$$I^g = I_f\left(m_h^2/(4m_t^2), 0\right) + \left(1 + \frac{11}{4}\frac{\alpha_s}{\pi}\right) \tag{2.7}$$

with

$$I_f(a,b) = \int_0^1 dx \int_0^{1-x} dy \frac{1-4xy}{1-4(a-b)xy-4by(1-y)} \tag{2.8}$$

$$I^g = \left(1 + \frac{11}{4}\frac{\alpha_s}{\pi}\right) \int_0^1 dx \int_0^{1-x} dy \frac{1-4xy}{1-\left(m_h^2/m_t^2\right)xy} \tag{2.9}$$

Compared to the SM, the total cross-section in the Standard Model EFT is rescaled by[32, 37]

$$\frac{\sigma(gg \to H)}{\sigma^{SM}(gg \to H)} \simeq \left|1 - \frac{8\pi^2 v^2 C_{HG}}{\Lambda^2 I^g}\right|^2 + \left|\frac{8\pi^2 v^2 C_{H\tilde{G}}}{\Lambda^2 I^g}\right|^2 \tag{2.10}$$

We see that we have also the contribution coming from CP-violating Lorentz operator $Q_{H\tilde{G}}$ which does not interfere with the SM amplitude[7]. The decay of $H \to gg$ which is not observable at the LHC[32] proceeds through the same diagrams if initial and final state gluon emission is neglected and it is modified by the same relative correction:

$$\frac{\Gamma(H \to gg)}{\Gamma^{SM}(H \to gg)} \simeq \frac{\sigma(gg \to H)}{\sigma^{SM}(gg \to H)} \tag{2.11}$$

In SM at one loop, the partial width of the Higgs decay into two photons is [32, 27]

$$\Gamma^{SM}(H \to \gamma\gamma) = \frac{\sqrt{2}\hat{G}_F \hat{\alpha}^2 \hat{m_h}^3}{16\pi^3} |I^\gamma|^2 \tag{2.12}$$

where I^γ is a Feynman parameter integral which has both contributions from the top quark(with leading QCD corrections) and W-boson loops [7]

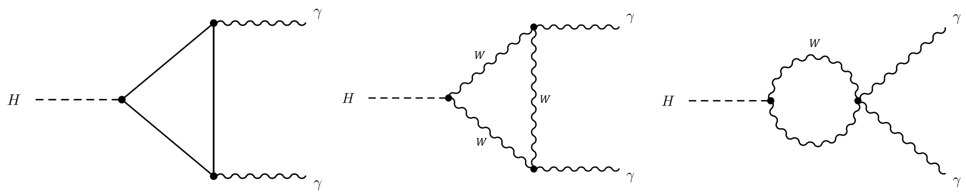

Figure 2.2: LO Feynman diagram for Higgs boson decaying into a pair of photons.

as one can have a look in Figure 2.2. At tree level in the SMEFT, the decay rate is modified as [32]

$$\frac{\Gamma(H \to \gamma\gamma)}{\Gamma^{SM}(H \to \gamma\gamma)} \simeq \left|1 - \frac{4\pi^2 v^2 C_{\gamma\gamma}}{\Lambda^2 I^g}\right|^2 + \left|\frac{4\pi^2 v^2 \tilde{C}_{\gamma\gamma}}{\Lambda^2 I^g}\right|^2 \tag{2.13}$$

Where

$$C_{\gamma\gamma} = C_{HW} + C_{HB} - C_{HWB} \tag{2.14}$$

$$\tilde{C}_{\gamma\gamma} = C_{H\tilde{W}} + C_{H\tilde{B}} - C_{H\tilde{W}B} \tag{2.15}$$

The Standard Model amplitude according to [32]

$$I^{\gamma} = I_W^{\gamma}\left(m_h^2/(4m_W^2), 0\right) + N_c Q_t^2 I_f\left(m_h^2/(4m_W^2), 0\right)\left(1 - \frac{\alpha_s}{\pi}\right) \tag{2.16}$$

where the fermion loop is dominated by top quark. The Feynman parameter integral is defined as:

$$I_W^{\gamma}(a,b) = \int_0^1 dx \int_0^{1-x} dy \frac{-4 + 6xy + 4axy}{1 - 4(a-b)xy - 4by(1-y)} \tag{2.17}$$

In equation (2.16) $N_c = 3$ is number of colors and $Q_t = 2/3$ is the top quark charge. In the limit $\frac{m_h}{m_W} \to 0$ one gets the well-known result $I_W^{\gamma}(0,0)$ = -7/4. For analytic expression of the $I_W^{\gamma}(a,b)$ one can check [27].

2.4 SMEFT at NLO

When we work at NLO, in order to obtain IR safe expression, we need to take into account the virtual corrections and real contributions. Starting from NLO, also partonic channels with a quark in the initial state contribute[34]. The NLO cross-section σ_{NLO} can be split into the LO cross-section , the virtual corrections $\Delta\sigma_{virtual}$ and the real corrections $\Delta\sigma_{real}$. The NLO result for the gluon-fusion cross-section for a single Higgs production can be expressed as [26]:

$$\sigma_{NLO}(pp \to H + X) = \sigma_{LO} + \Delta\sigma_{virtual} + \Delta\sigma_{gg} + \Delta\sigma_{q\bar{q}} + \Delta\sigma_{qg} \tag{2.18}$$

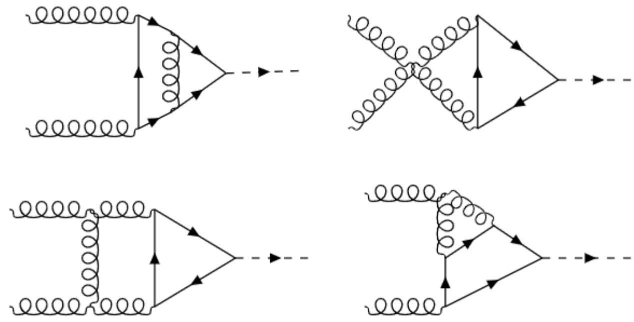

Figure 2.3: Partial generic Feynman diagrams for the virtual corrections to LO process $\mathbf{gg} \to \mathbf{H}$ which appear as two-loops contributions.

where, $\Delta\sigma_{gg} + \Delta\sigma_{q\bar{q}} + \Delta\sigma_{qg}$ are real contributions. As we saw in the beginning, dealing with gluon fusion as the main production channel, the LO cross-section is already a loop-induced process so the virtual corrections are two-loop contributions with two gluons in the initial state (see Figure 2.3). The real corrections are one-loop contributions with two gluons, a gluon and anti-quark or quark and antiquark in the initial state (see Figure 2.4. The goal of this master thesis is to consider the phenomenological impact of the NLO corrections coming from these operators by using MADGARPH5_AMC@NLO presented in[25]. Regarding the contributions which are coming from the operators $\mathcal{O}_1, \mathcal{O}_2, \mathcal{O}_3$ that we deal in our work (see Figure 2.1). Contributions from $\mathcal{O}_1$ (see Figure 2.1 orange blob) which presents direct coupling of Higgs with gluons something which is not presented in SM, however, NLO contributions coming from this operator are known because the NLO contributions are proportional to the NLO corrections to gluon-fusion in the SM where the top quark is integrated out [13]. Since the contribution coming from $\mathcal{O}_2$ (see Figure 2.1 purple blob) is proportional to the SM amplitude, the NLO corrections can be obtained from NLO corrections to gluon-fusion in the SM considering the full mass of the top quark [16, 15, 11, 8]. While the NLO contributions coming from $\mathcal{O}_3$ (see Figure 2.1 blue blob) are presented in [34, 30].

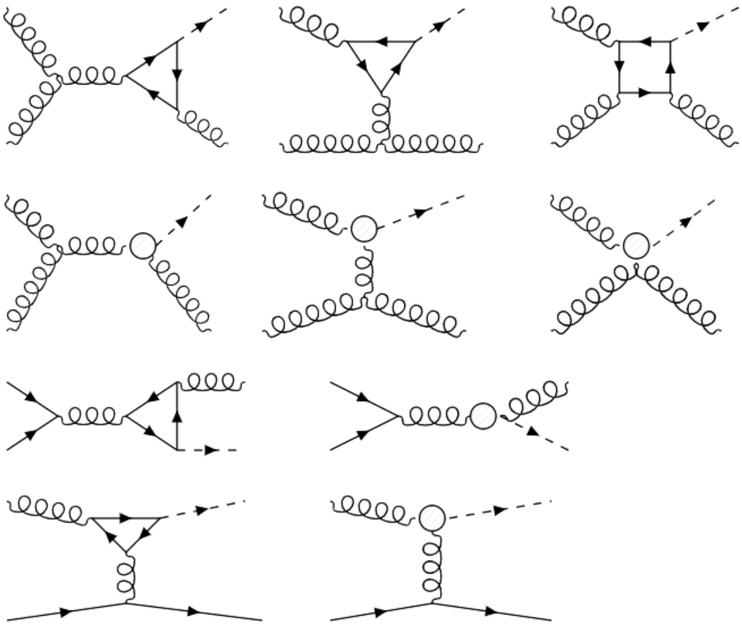

Figure 2.4: Partial Feynman diagrams for real corrections to LO process $\mathbf{gg \to Hg, q\bar{q} \to Hg, qg \to Hq}$ which appear as 1-loop contributions. The Blobs represent contributions that turn to contact interaction between gluons and Higgs when we integrate out the top quark.

Chapter 3

Results

In this chapter, we present the effect of the Wilson coefficients relevant for the Higgs. We start with a brief description of the automation of the computations of next-to-leading order cross sections by `MADGRAPH5_aMC@NLO` and the parametrization of the cross-section from dimension-six operators, moving forward to differential distributions of the observables like transverse momentum and rapidity.

3.1 Automation of the computations of NLO cross-section results

This section will cover briefly the documentation for the basic running of the code in `MADGRAPH5_aMC@NLO`, which is a framework that aims at providing all the elements necessary for SM and BSM phenomenologies, such as the computations of cross-sections, the generation of hard events and their matching with event generators, and the use of a variety of tools relevant to event manipulation and analysis. Processes can be simulated to NLO accuracy in the case of QCD corrections to SM processes. Computation of a cross-section by `MADGRAPH5_aMC@NLO` consists of three steps:*generation*, *output* and *running* as presented in [25]. For the NLO QCD generation, we have used the `SMEFT@NLO` model, described as:

```
import model SMEFTatNLO_U2_2_U3_3_cG_4F_LO_UFO-NLO
```

which is the NLO restriction card. For NLO QCD generation, the NLO restriction card should be used in order to import the model, such that we can access SMEFT interactions. In the generation phase, since we were interested in the gluon-fusion process for $H + 1j$ we have generated the event as follows:

```
generate g g > H j NP=2 [noborn=QCD]
output ggF-SMEFTatNLO_1j
```

where `ggF-SMEFTatNLO_1j` is a name we have chosen for the process with

1 jet that MADGRAPH5_aMC@NLO will, in turn, assign to the directory under whose tree the cross-section of the process just generated is written. Same we have done for ggF-SMEFTatNLO_0j, but separately. In our simulation, we have simulated zero-jet and one-jet separately and after generating 100,000 events for each process, by creating 100 Rivet.yoda files for zero-jets and 100 others Rivet.yoda files for one-jets. Afterwards, using yodamerge script, histograms from these two different Rivet runs will merge into a single one. This is done to get a significant amount of one-jet event, because otherwise if we just let MADGRAPH5_aMC@NLO run the two processes for zero and one jet together will result in a higher number of zero-jets and fewer 1-jets. This would cause that a statistical uncertainty in 1-jet phase space to be much larger than 0-jet, therefore, we proceed such that two processes are simulated independently. Besides, to simulate accurately an LHC collision we have also to account for the Parton Distribution Function(PDF) of the proton as well the showering and hadronization. Therefore, for the description of the observables, we match our NLO predictions to the parton shower with MC@NLO method [42, 25], and we use PYTHIA8[1] for the parton shower. Finally, the events are analyzed with the Rivet package [3] which makes the validation of Monte Carlo (MC) event generators. Rivet uses Yoda as the main histogramming system by creating histograms files as Rivet.yoda. Moreover, we modified a routine that simulates the real event selections performed in the CMS analysis. The selection of the event is done respecting the detector acceptance (photon with$|\eta| < 2.5$, jets with $p_T > 30GeV$ and $|\eta| < 4.7$). In figure 3.1 we can see the statistical precision that we obtained for the transverse momentum based on the choice of the binning:
[0,10,20,30,40,50,70,90,100,150,200,250,300,400,500]. The binning arrangement led to the relative uncertainty below 10%. We can see that for transverse-momentum around $400GeV$ the relative uncertainty grows to 6%. Regarding the treatment that we have done to the decay, the Branching Ratio (BR) remained unchanged because of the limitations within the model. This means that the effect of the dimension-six operators it is not considered on the decay of Higgs into pairs of photons, however, if the dimension-six operator effect was included this would result in the change of the Branching Ratio and not the kinematics.

The effect of the dimension-six SMEFT operators on cross-sections, differential distributions, or other observables, can be written as

$$\sigma_{SMEFT} = \sigma_{SM} + \sum_{i}^{n_d} \sigma_i \frac{C_i}{\Lambda^2} + \sum_{i,j}^{n_d} \tilde{\sigma}_{ij} \frac{C_i C_j}{\Lambda^4} + ..., \tag{3.1}$$

where the first term denotes the SM prediction, second term interference between the SM and dimension-six SMEFT operators and the last term interaction of the operators with each other.

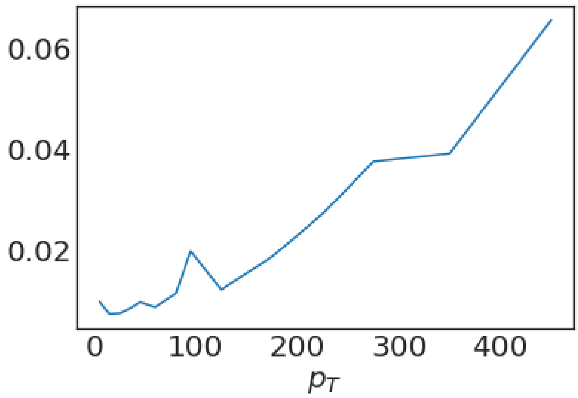

Figure 3.1: Statistical precision of Higgs p_T observable.

Although there is a possibility that we have simultaneous variations of two or three operator coefficients like in [29], in this study we focus on the impact that each operator has on the chosen observables in a range of $0 > p_T > 500GeV$, hence we vary them one by one while keeping the others to SM value (i.e. to zero). Operator coefficients that we vary in this master thesis are cpg, ctp, ctg, and cpbb. These are dimensionless coupling coefficients or Wilson coefficients which determine the interaction strength of the effective operators $\mathcal{O}_1$, $\mathcal{O}_2$, $\mathcal{O}_3$, $\mathcal{O}_4$. They contain all the pieces of information about short-distance physics above the SM scale, hence they are sometimes called short-distance coefficients. Relation of the Operators to the coefficients it is visible in the Table 3.1. Regarding the variation, we perform a scan in the step of 0.2 (which is an arbitrary choice), and limiting to 10 points (5 positive and 5 negative), which was for a practical reason because the results can be produced for any value. We use a variation of these short-handed coefficients coefficients and we look on their effect on this choice of variables:

$p_T^{\gamma\gamma}$- the transverse momentum spectrum of the diphoton pair, i.e. of the Higgs boson itself.

$p_T^{\gamma_1}$- the transverse momentum spectrum of the first photon.

$p_T^{\gamma_2}$- the transverse momentum spectrum of the second photon.

p_T^{jet} - transverse momentum spectrum of the jet with the highest transverse momentum in the event (considering only jets with $|\eta| < 2.5$).

N_{jets} - number of jets in the event with $|\eta| < 2.5$ and $p_T > 30GeV$.

Operator	Operator coefficient
$\mathcal{O}_1 = \lvert H\rvert^2 G^a_{\mu\nu} G^{a,\mu\nu}$	**cpg**
$\mathcal{O}_2 = \lvert H\rvert^2 \bar{Q}_L H^c t_R + h.c.$	**ctp**
$\mathcal{O}_3 = \bar{Q}_L H \sigma^{\mu\nu} T^a t_R G^a{}_{\mu\nu} + h.c.$	**ctg**
$\mathcal{O}_4 = \lvert H\rvert^2 B_{\mu\nu} B^{\mu\nu}$	**cpbb**

Table 3.1: Relation of the operator to the coefficient.

3.2 Chi-Squared Distance Metric

As a metric, we have used χ^2 (chi-squared) metric to check the comparison of Histogram data. The standard metric is defined as

$$\chi^2 = \frac{(h_1 - h_i)^2}{\sigma^2} \tag{3.2}$$

where the h_1 denotes the expected values (SM), h_i number of simulating events found in the bins for different variations values of the single coefficient, σ^2 is the variance of h_1 for each bin, $\sigma = \sqrt{h_1}$. Equation 3.2 represent the standard chi-square metric which affects the normalization and the shape variations, whereas the normalized chi-square affects only the shape variations. The normalized chi-square is computed in the same way as the standard χ^2. The difference lies in the fact that h_1 and h_i histograms are normalized to have the same area (i.e. same cross-section), in this way any impact on the total cross-section is factorized and the normalized chi-square value provides a piece of direct information on the shape difference. We have used this metric to evaluate the impact that operators have on different observables. With the help of chi-square, we will obtain numbers which tell us which observable is most sensitive to a given operator. Histograms that give larger chi-square values indicate bigger impact, while the smaller the value of the chi-square the smaller is the impact or the observable is less sensitive to this given value of the operator coefficient. Histograms that have negative values give zero chi-square values and cannot be log-scaled. Chosen values for the impact of the operator on the observables are shown in the Tables 3.2 to 3.5.

Observable	Coefficient values	χ^2	Normalized χ^2
$p_T^{\gamma\gamma}$	cpg=-1.0	201253283	10280
	cpg=-0.2	14473	14473
	cpg=1.0	342276543	9919
	cpg=0.2	622011	10316
$p_T^{\gamma_1}$	cpg=-1.0	188744678	2238
	cpg=-0.2	15961	8627
	cpg=1.0	321910407	2217
	cpg=0.2	547917	2477
$p_T^{\gamma_2}$	cpg=-1.0	189150191	2510
	cpg=-0.2	16995	10866
	cpg=1.0	322488722	2445
	cpg=0.2	550333	2734
p_T^{jet}	cpg=-1.0	187209914	5799
	cpg=-0.2	21265	20654
	cpg=1.0	319261206	5454
	cpg=0.2	563012	5645
N_{jets}	cpg=-1.0	185014618	49
	cpg=-0.2	13388	2971
	cpg=1.0	315770375	92
	cpg=0.2	526084	285

Table 3.2: Impact of the operator coefficient cpg on observables.

Observable	Coefficient values	χ^2	Normalized χ^2
$p_T^{\gamma\gamma}$	ctp=-1.0	98697	5316
	ctp=-0.2	109983	5316
$p_T^{\gamma_1}$	ctp=-1.0	98747	701
	ctp=-0.2	110081	701
$p_T^{\gamma_2}$	ctp=-1.0	98746	751
	ctp=-0.2	110080	751
p_T^{jet}	ctp=-1.0	94613	1586
	ctp=-0.2	105566	1586
N_{jets}	ctp=-1.0	98760	1764
	ctp=-0.2	110084	1764

Table 3.3: Impact of the operator coefficient ctp on observables.

Observable	Coefficient values	χ^2	Normalized χ^2
$p_T^{\gamma\gamma}$	ctg=-0.2	2578	157
	ctg=0.2	3530	113
	ctg=1.0	83787	1080
$p_T^{\gamma_1}$	ctg=-0.2	2490	19
	ctg=0.2	3409	13
	ctg=1.0	142041	170
$p_T^{\gamma_2}$	ctg=-0.2	2491	20
	ctg=0.2	3410	14
	ctg=1.0	142089	182
p_T^{jet}	ctg=-0.2	2446	45
	ctg=0.2	3349	32
	ctg=1.0	139529	401
N_{jets}	ctg=-0.2	2513	54
	ctg=0.2	3442	39
	ctg=1.0	143429	512

Table 3.4: Impact of the operator coefficient ctg on observables.

Observable	Coefficient values	χ^2	Normalized χ^2
$p_T^{\gamma\gamma}$	cpbb=-0.66	6602	508
	cpbb=0.66	11282	291
	cpbb=3.3	609617	2493
$p_T^{\gamma_1}$	cpbb=-0.66	6373	64
	cpbb=0.66	10895	35
	cpbb=3.30	588902	292
$p_T^{\gamma_2}$	cpbb=-0.66	6378	73
	cpbb=0.66	10903	40
	cpbb=3.30	589393	341
p_T^{jet}	cpbb=-0.66	6248	144
	cpbb=0.66	10679	80
	cpbb=3.30	577101	668
N_{jets}	cpbb=-0.66	6431	176
	cpbb=0.66	10999	103
	cpbb=3.30	594773	902

Table 3.5: Impact of the operator coefficient cpbb on observables.

3.3 Differential distributions from:$\mathcal{O}_1$,$\mathcal{O}_2$,$\mathcal{O}_3$,$\mathcal{O}_4$

We perform our analysis by looking only to contributions of exactly one operator coefficient for the relevant observables of the Higgs Boson. In figure 3.2 we see non-normalized contribution in Higgs transverse momentum for the overall cross-section and the ratio, while in figure 3.3 we see the shape distribution for the normalized case. In the coming pages of this work to avoid the redundancy, only the overall cross-section variation on normalization and the normalized ratio focusing on the tails will be shown. Looking at p_T interval $(0GeV \leq p_T \leq 500GeV)$ in Figures 3.3-3.12 direct coupling of Higgs with gluons modifies the spectrum at large transverse momenta as expected. We stop at 500 GeV because this is a range which is accessible today. To see the impact of the coefficient operators on the observables we compare the chi-squared values. First, we compare the chi-square for the same value of the coefficient but different observable. Then chi-square difference between different coefficient values but the same observable.

From Table 3.2 we can see the impact of cpg operator coefficient on the observables. We take into consideration the fact that bigger the chi-square value bigger the impact or observable is more sensitive to a given value of the operator coefficient. We can see that for positive (negative) values of cpg=1.0 (cpg=-1.0) the observable with the highest chi-square value is $p_T^{\gamma\gamma}$ (see Fig.3.3 and 3.4). This means that this observable is the most sensitive one from all other observables present in this table. On the other hand, for positive (negative) value variations cpg=0.2 (cpg=-0.2) the observable with the lowest chi-square value is N_{jets} (see Fig.3.11 and3.12). Therefore, this observable is the less sensitive one for this given value from all other observables present in the table for cpg variation. If we look for different values of the operator coefficient like(0.2,-0.2,1.0,-1.0) but the same observables then this follows:

$p_T^{\gamma\gamma}$ is most sensitive for the value cpg=1.0 (see Fig.3.3) followed by negative value cpg=-1.0 and ending with the less sensitive one cpg=-0.2. Therefore the biggest impact of the operator coefficient values it is coming from the highest positive value of cpg, respectively cpg=1.0. Other observables are seen in Table 3.2 are mostly affected by the positive values of cpg, which means these values give the biggest chi-square numbers. Speaking of the negative value the biggest impact is coming from cpg=-1.0 (see Fig.3.4). However, the behaviour of the spectrum is different from the negative value contribution. From the differential distributions coming from the cpg, negative values harden the spectrum more than positive values. Where negative values distributions at high transverse momentum tail go above the SM(solid, red) while positive values hardly exceed the SM contributions coming from ($\mathcal{O}_1$) operator, see Figures 3.3-3.12.

From Table 3.3 we can see the impact of ctp values on the observables. In our case observables were sensitive only to the negative variations of the ctp, because histograms do not appear for positive value variations, which means have negative value and cannot be log-scaled, leading to zero chi-square values. To explain the impact that this operator coefficient have on observable we concentrate on large values of the chi-square. Generally, observables are more sensitive to ctp=-0.2 value rather than ctp=-1.0, because for ctp=-0.2 chi-square values are higher than for ctp=-1.0 (see Table 3.3). The most sensitive observable from Table 3.3 is N_{jets} (see Fig.3.17). If we compare the chi-square for ctp=-1.0 and different observable, N_{jets} results to be the observable which feels the biggest impact above other observables followed by $p_T^{\gamma_1}$ (see Fig. 3.14) and ending with less sensitive for ctp=-1.0, observable p_T^{jet} (see Fig.3.16). However, looking at the transverse momentum interval $(0GeV \leq p_T \leq 500GeV)$ from the 3.13 to 3.17 modification of the top Yukawa alone without simultaneous variations with other six-dimension operators will lead to the effects of the rescaling the total cross-section, respectively affecting the normalization. The variations of the coefficients hardly produce effects that exceed the NLO predictions keeping the total rate close to it. If there would be simultaneous variations of ctp with other operators like in [29] there will be a compensation between interference terms and squared contribution of the operator with itself leading to the significant deformation of the spectrum.

From Table 3.4 we can see the impact of ctg operator coefficient on the observables. For variation value of ctg=1.0 the observable with the biggest chi-square is N_{jets} (see Fig.3.22), explaining that this observable is the most sensitive one among all observables in Table 3.4. For positive (negative)value variations cpg=0.2(cpg=-0.2) the observable with the lowest chi-square value is p_T^{jet} (see Fig.3.21). Comparing negative variations values with positive ones, we see that the positive variation of the operator coefficient has a bigger impact on observables than a negative ones. Looking for different coefficient values but same observable (see Figures 3.18 to 3.22) we witness that the observables follow the same practice, being most sensitive for ctg=1.0 rather than ctg=0.2 and less for ctg=-0.2.

Concentrating on the CP conserving operator ($\mathcal{O}_4$) the variation for the same values as operator coefficients mentioned above i.e. 0.2 to 1.0 it is not relevant, better to say chi-square values are zero or no sensitivity shown. The impact of cpbb on observables is visible in Table 3.5. The observable $p_T^{\gamma\gamma}$ is the most sensitive one (see Fig.3.23), which for a given value of cpbb=3.30 gives the largest chi-square value among all observables, ending with less sensitive observable p_T^{jet} for cpbb=-0.66 (see Fig.3.26). For positive(negative) values cpbb=0.66 (cpbb=-0.66) the chi-square with the largest value is present to $p_T^{\gamma\gamma}$ observable. On the whole, the biggest impact is coming from positive values of operator coefficient (i.e. cpbb=3.30), which result in larger chi-square value, rather than negative ones. The behaviour of the spectrum is visible on the distributions from Fig.3.23 to 3.27.

Besides looking for the same operator coefficient and different observables we can also check the different operator coefficient for fixed value and looking in the same observable. In this way, we find which of the operator coefficients affects specific observable the most.

We start with operator coefficient variations of cpg, ctp, ctg =-0.2. For this given value the largest chi-square is coming from modification of the top Yukawa operator coefficient (ctp) followed by direct coupling of Higgs with gluons (cpg) and ending with chromomagnetic operator coefficient (ctg), which results on the lowest chi-square values. Therefore, from these three operator coefficients value, ctp has the biggest impact on the N_{jets} observable.This practice is relevant for other observables, meaning that ctp has the biggest impact on other observables too. Regarding the arrangement of sensitivity the leading observable is N_{jets} as the most sensitive one (see Fig.3.17), followed by p_T^{jet} (see Fig.3.16) as the less sensitive one for this given value of the ctp coefficient.

For ctp, cpg = -1.0, the largest chi-square value is coming from direct coupling of Higgs with gluons, which means that the latter operator coefficient has bigger impact on the observables compared to the modification of the top Yukawa. The biggest impact is present on $p_T^{\gamma\gamma}$ observable. This signature is followed also for other observables where cpg dominates compared to ctp for -1.0 variation value. This sensitivity starts with observable $p_T^{\gamma\gamma}$ (see Fig.3.4) which is the most sensitive followed by, $p_T^{\gamma_2}$, $p_T^{\gamma_1}$, p_T^{jet} (see Fig.3.7, 3.5 and 3.9) and the last one N_{jets} (see Fig.3.11).

Regarding, the variation cpg, ctg = 0.2, direct coupling of Higgs with gluons has a bigger impact on observables because the chi-square values for the relevant observables are higher compared to the values of chromomagnetic operator coefficient. This custom is implemented same for other observables where the cpg=0.2 has a bigger impact on all other observables than ctg=0.2. This sensitivity starts with observable $p_T^{\gamma\gamma}$ as the most sensitive one (see Fig.3.3) followed by p_T^{jet} , $p_T^{\gamma_2}$, $p_T^{\gamma_1}$(see Fig.3.10, 3.8 and 3.6) and ending with less sensitive one N_{jets} (see Fig.3.12).

In addition, for ctg, cpg = 1.0, again direct coupling of Higgs with gluons dominates over chromomagnetic operator. Based on the chi-square values we find that cpg affects observables more than ctg for this given value of the coefficients. The most sensitive observable results to be the one with the highest chi-square value which is $p_T^{\gamma\gamma}$ (see Fig.3.3). This signature is followed by $p_T^{\gamma_2}$, $p_T^{\gamma_1}$, p_T^{jet} (see Fig.3.8, 3.6 and 3.10), ending with the less sensitive one for cpg=1.0 the observable N_{jets} (see Fig.3.12). However, this latter contribution of cpg for N_{jets} is still dominant over chromomagnetic operator contribution. Because when we do comparison of ctg and cpg for a 1.0 variation value, the smallest impact is present on $p_T^{\gamma\gamma}$ observable for ctg=1.0 (see Fig.3.18)

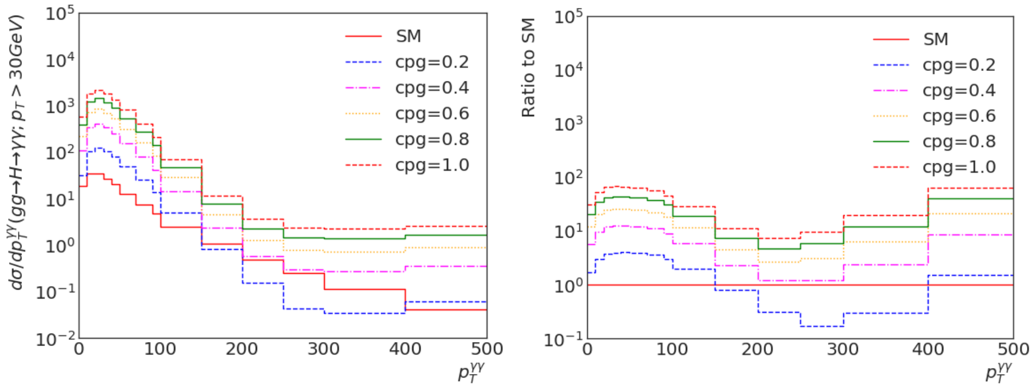

Figure 3.2: Standard Model (SM) contribution and individual operator contributions of $p_T^{\gamma\gamma}$ are displayed, for not normalized case.Right panel gives the ratio over the SM.

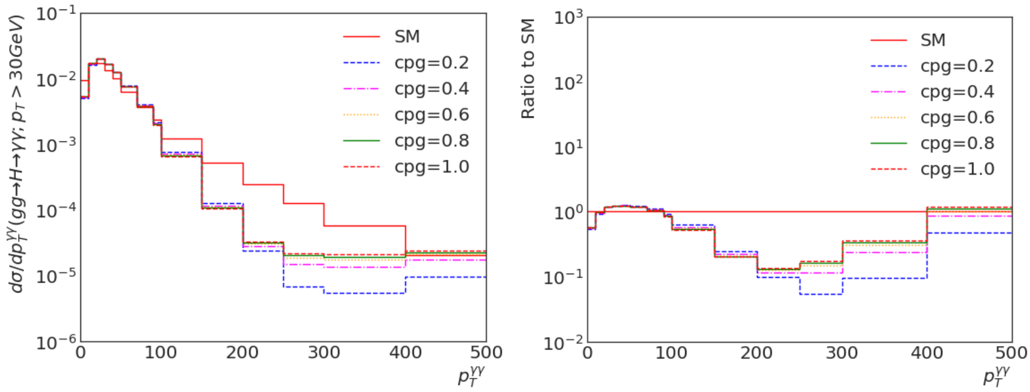

Figure 3.3: Standard Model (SM) contribution and individual operator contributions of $p_T^{\gamma\gamma}$ are displayed, for normalized case.Right panel gives the ratio over the SM.

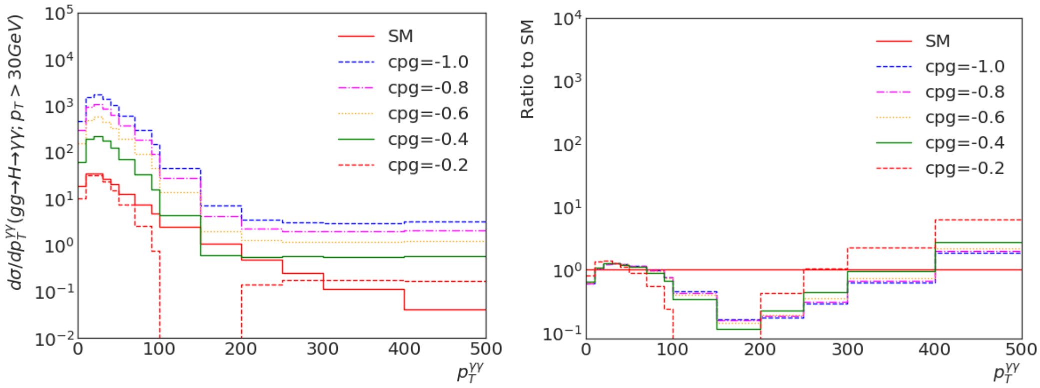

Figure 3.4: SM (red, solid) and negative cpg operator coefficient value contributions for $p_T^{\gamma\gamma}$. The right panel gives the normalized ratio with respect to the SM prediction

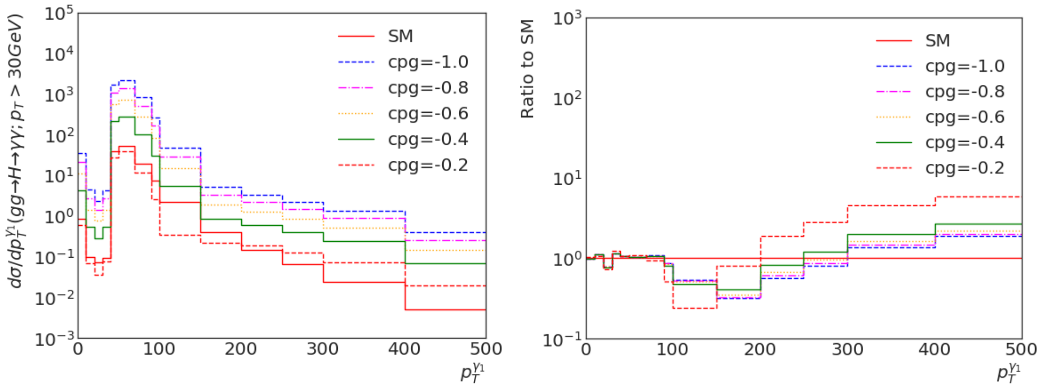

Figure 3.5: SM (red, solid) and negative cpg operator coefficient value contributions for $p_T^{\gamma_1}$. The right panel gives the normalized ratio with respect to the SM prediction

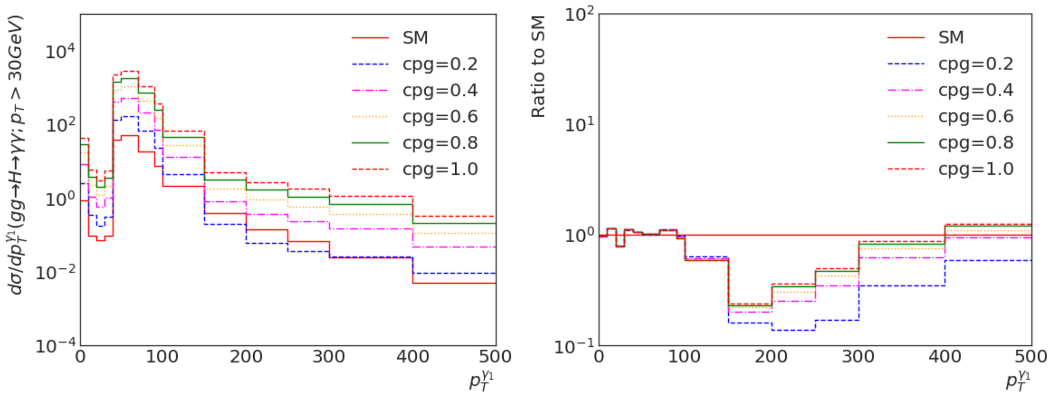

Figure 3.6: SM (red, solid) and positive cpg operator coefficient value contributions for $p_T^{\gamma_1}$. The right panel gives the normalized ratio with respect to the SM prediction

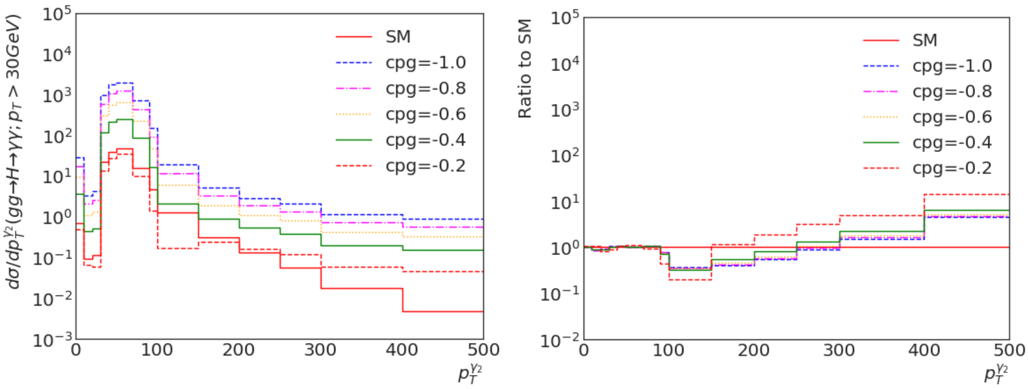

Figure 3.7: SM (red, solid) and negative cpg operator coefficient value contributions for $p_T^{\gamma_2}$. The right panel gives the normalized ratio with respect to the SM prediction

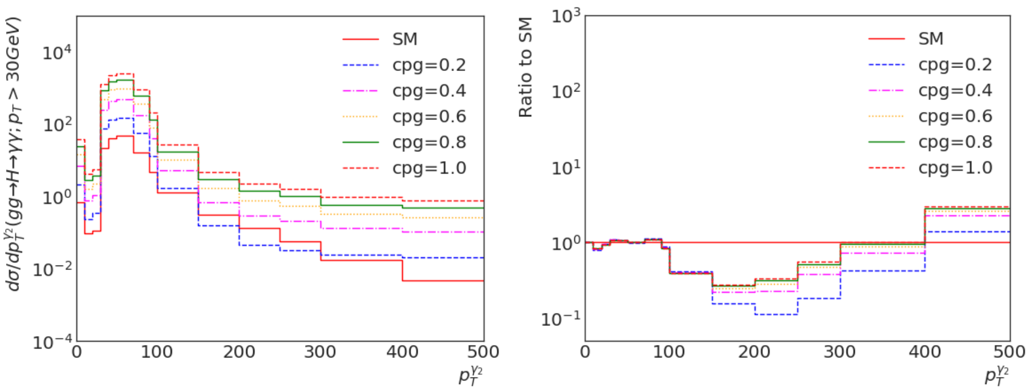

Figure 3.8: SM (red, solid) and positive cpg operator coefficient value contributions for $p_T^{\gamma_2}$. The right panel gives the normalized ratio with respect to the SM prediction

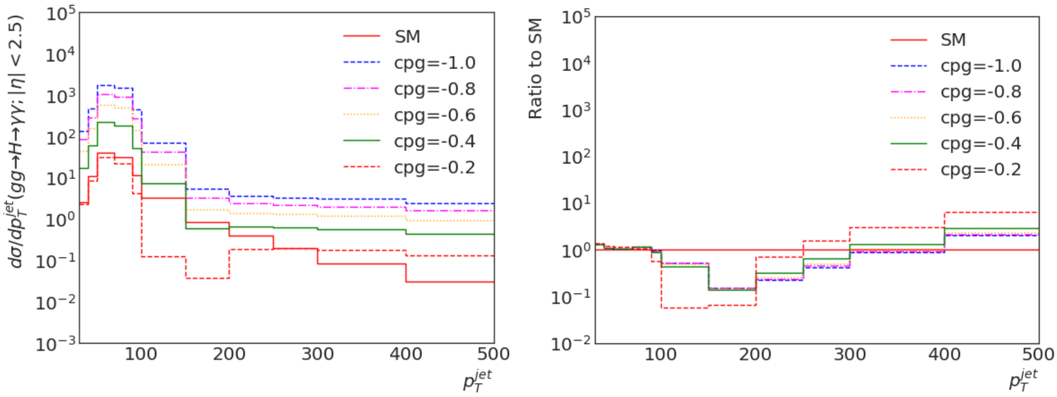

Figure 3.9: SM (red, solid) and negative cpg operator coefficient value contributions for p_T^{jet}. The right panel gives the normalized ratio with respect to the SM prediction

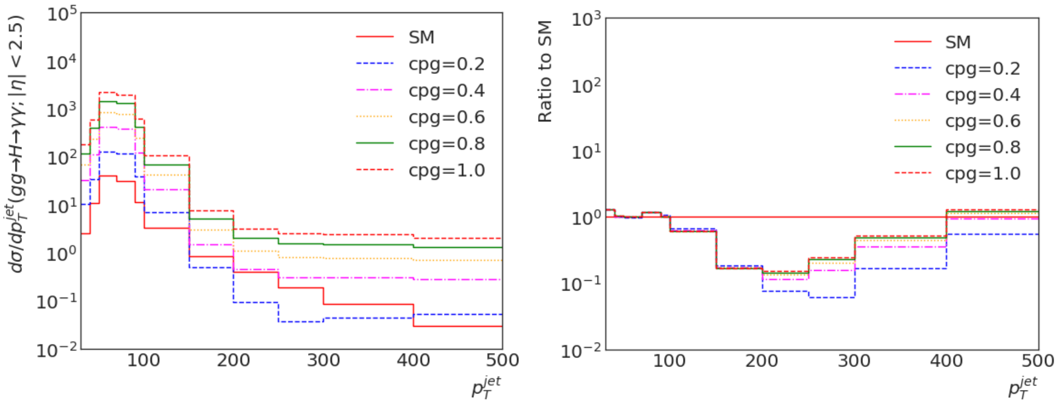

Figure 3.10: SM (red, solid) and positive cpg operator coefficient value contributions for p_T^{jet}. The right panel gives the normalized ratio with respect to the SM prediction

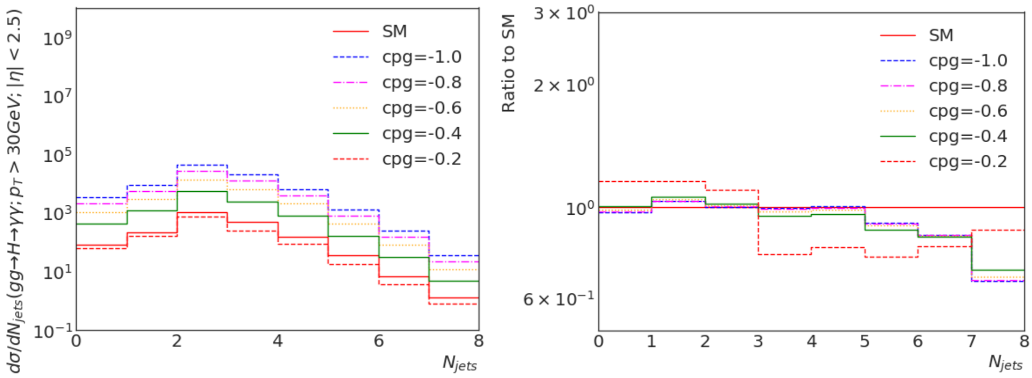

Figure 3.11: SM (red, solid) and negative cpg operator coefficient value contributions for N_{jets}. The right panel gives the normalized ratio with respect to the SM prediction

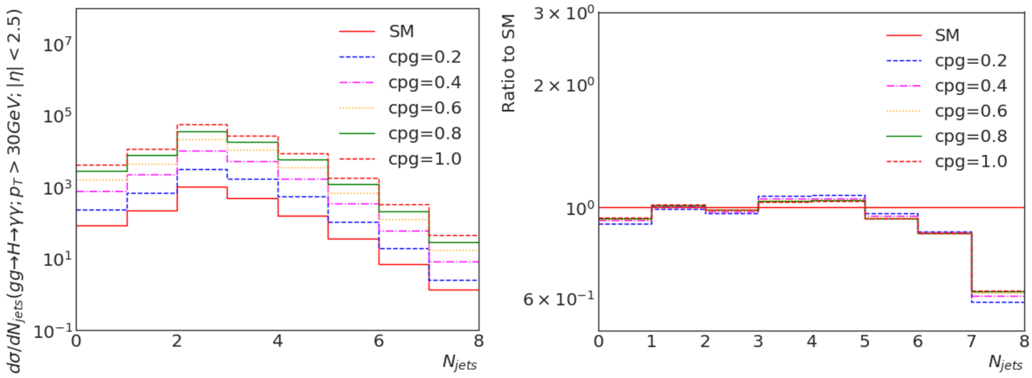

Figure 3.12: SM (red, solid) and positive cpg operator coefficient value contributions for N_{jets}. The right panel gives the normalized ratio with respect to the SM prediction

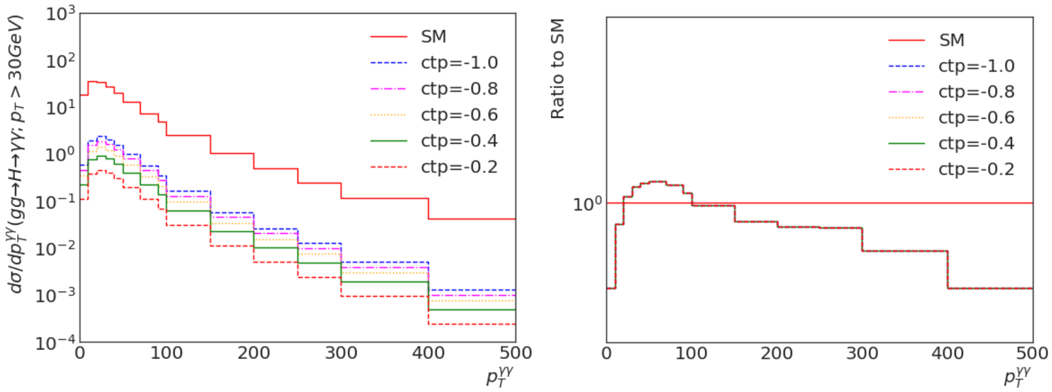

Figure 3.13: SM (red, solid) and negative ctp operator coefficient value contributions for $p_T^{\gamma\gamma}$. The right panel gives the normalized ratio with respect to the SM prediction

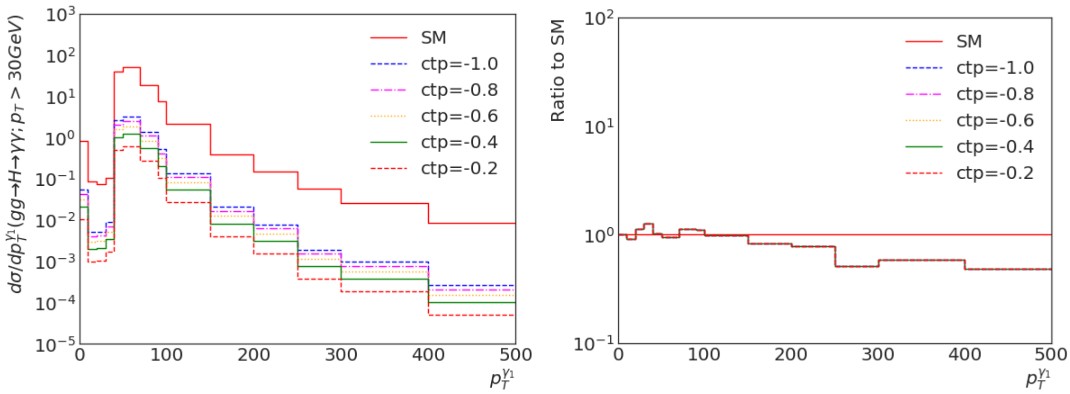

Figure 3.14: SM (red, solid) and negative ctp operator coefficient value contributions for $p_T^{\gamma_1}$. The right panel gives the normalized ratio with respect to the SM prediction

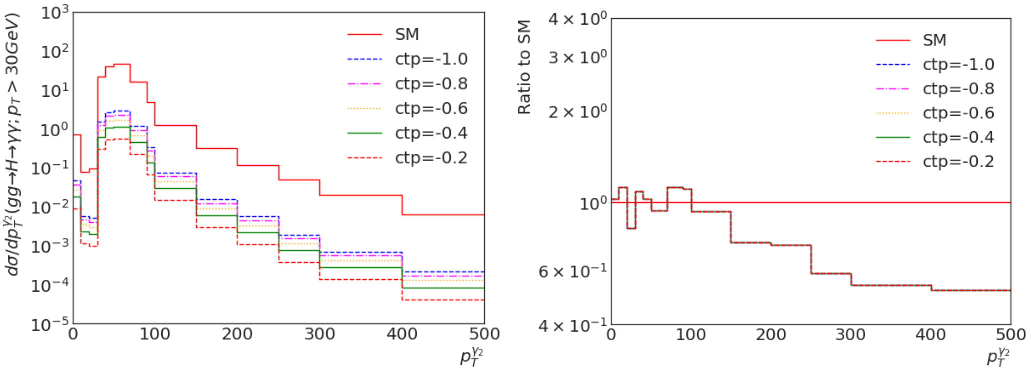

Figure 3.15: SM (red, solid) and negative ctp operator coefficient value contributions for $p_T^{\gamma_2}$. The right panel gives the normalized ratio with respect to the SM prediction

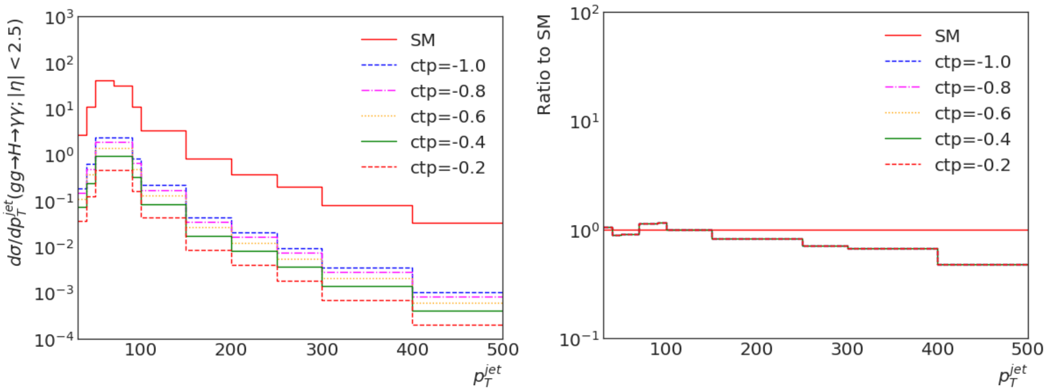

Figure 3.16: SM (red, solid) and negative ctp operator coefficient value contributions for p_T^{jet}. The right panel gives the normalized ratio with respect to the SM prediction

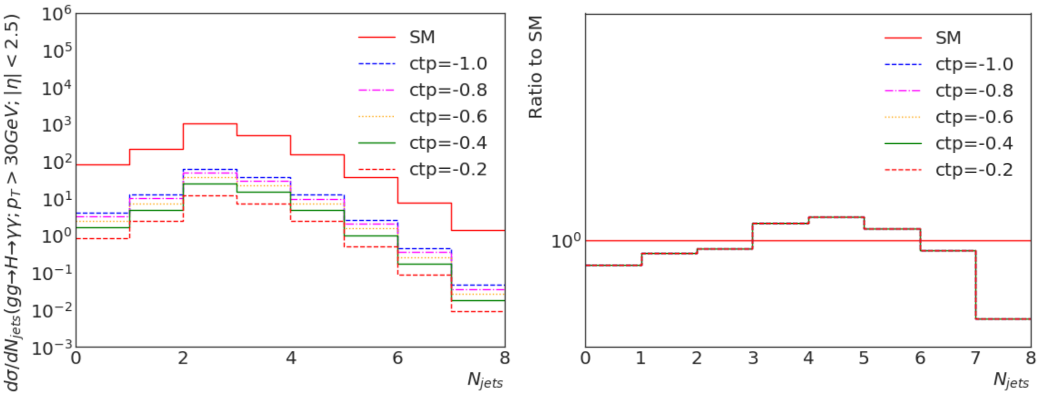

Figure 3.17: SM (red, solid) and negative ctp operator coefficient value contributions for N_{jets}. The right panel gives the normalized ratio with respect to the SM prediction

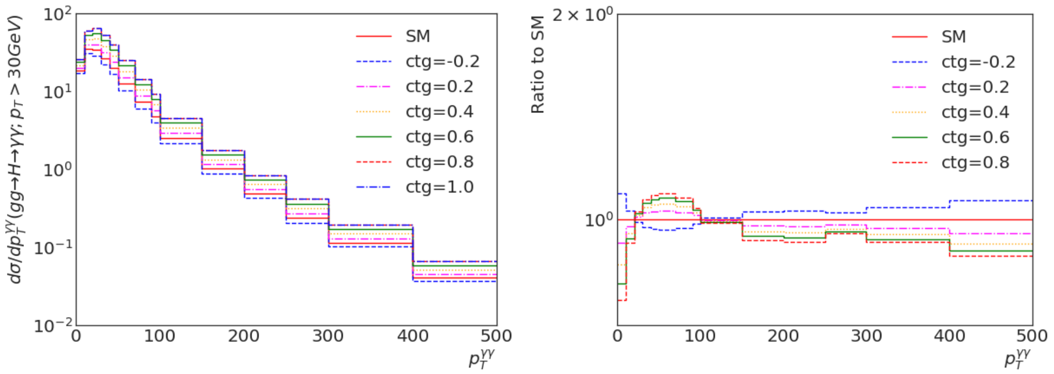

Figure 3.18: SM (red, solid) and ctg operator coefficient value contributions for $p_T^{\gamma\gamma}$. The right panel gives the normalized ratio with respect to the SM prediction

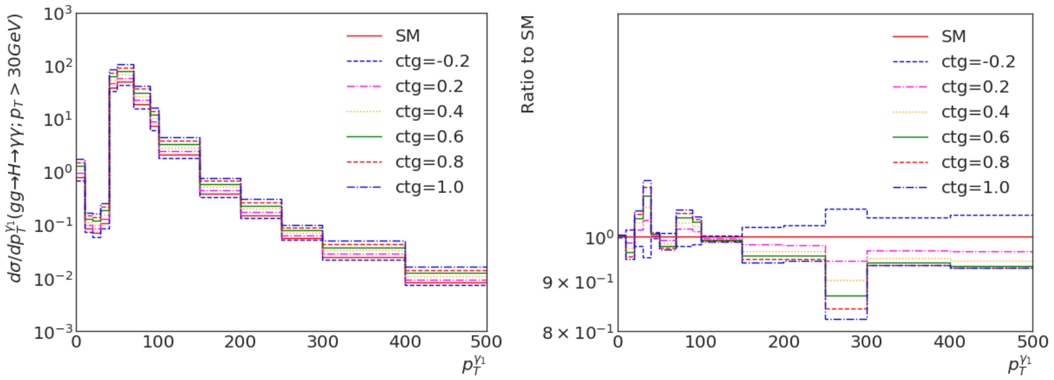

Figure 3.19: SM (red, solid) and ctg operator coefficient value contributions for $p_T^{\gamma_1}$. The right panel gives the normalized ratio with respect to the SM prediction

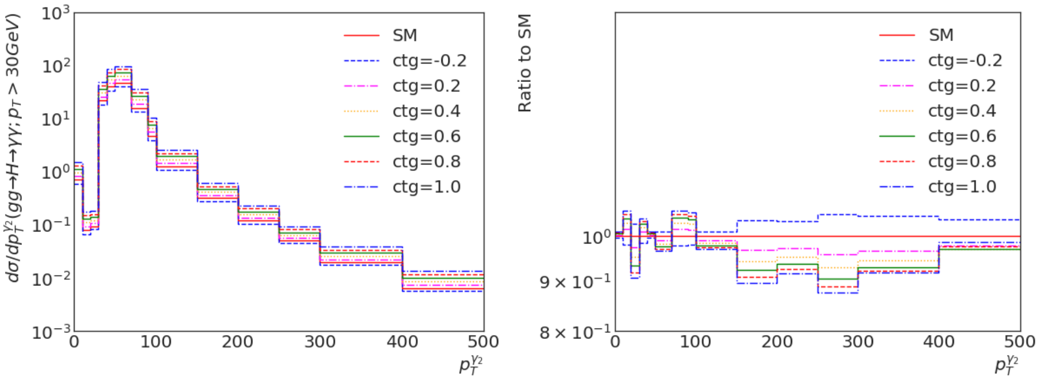

Figure 3.20: SM (red, solid) and ctg operator coefficient value contributions for $p_T^{\gamma_2}$. The right panel gives the normalized ratio with respect to the SM prediction

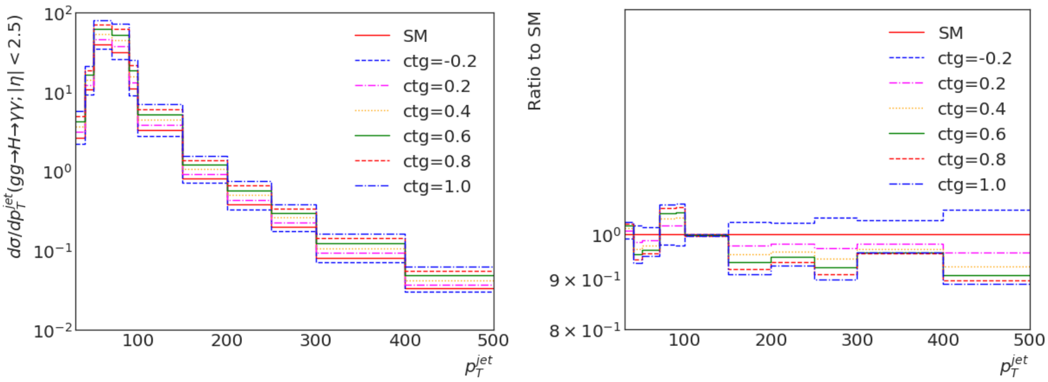

Figure 3.21: SM (red, solid) and ctg operator coefficient value contributions for p_T^{jet}. The right panel gives the normalized ratio with respect to the SM prediction

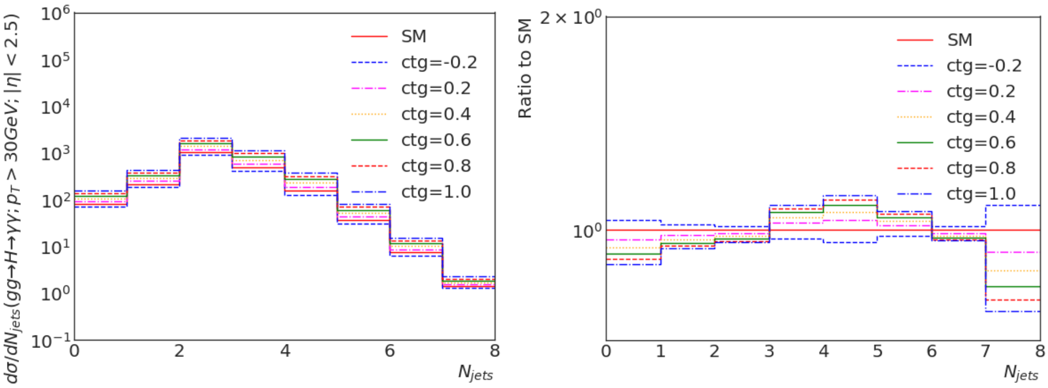

Figure 3.22: SM (red, solid) and ctg operator coefficient value contributions for N_{jets}. The right panel gives the normalized ratio with respect to the SM prediction

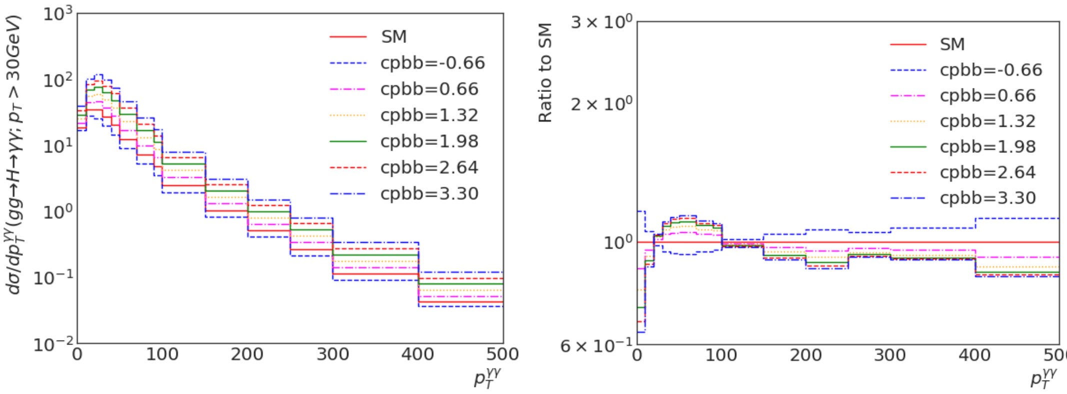

Figure 3.23: SM (red, solid) and cpbb operator coefficient value contributions for $p_T^{\gamma\gamma}$. The right panel gives the normalized ratio with respect to the SM prediction

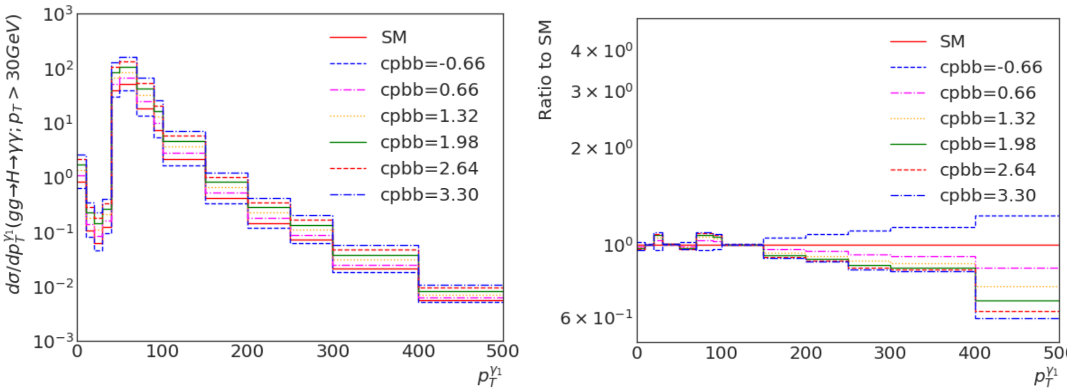

Figure 3.24: SM (red, solid) and cpbb operator coefficient value contributions for $p_T^{\gamma_1}$. The right panel gives the normalized ratio with respect to the SM prediction

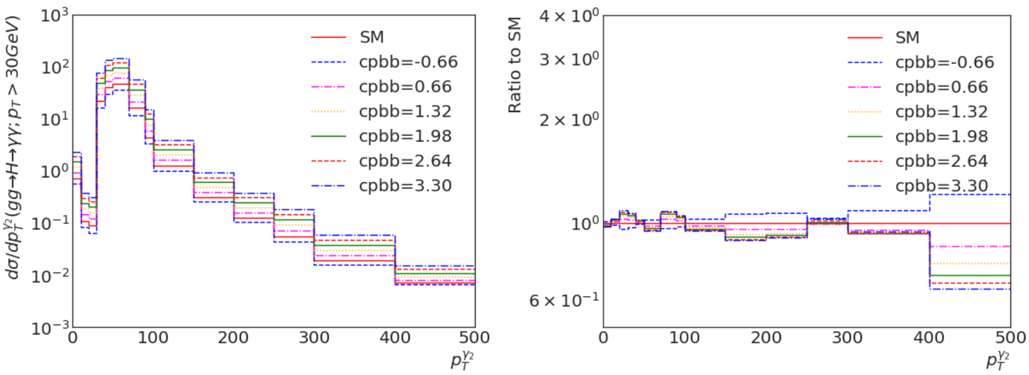

Figure 3.25: SM (red, solid) and cpbb operator coefficient value contributions for $p_T^{\gamma_2}$. The right panel gives the normalized ratio with respect to the SM prediction

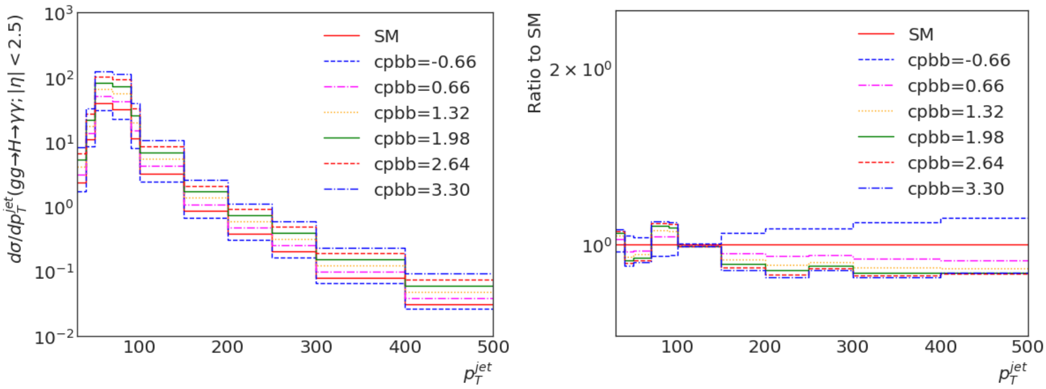

Figure 3.26: SM (red, solid) and cpbb operator coefficient value contributions for p_T^{jet}. The right panel gives the normalized ratio with respect to the SM prediction

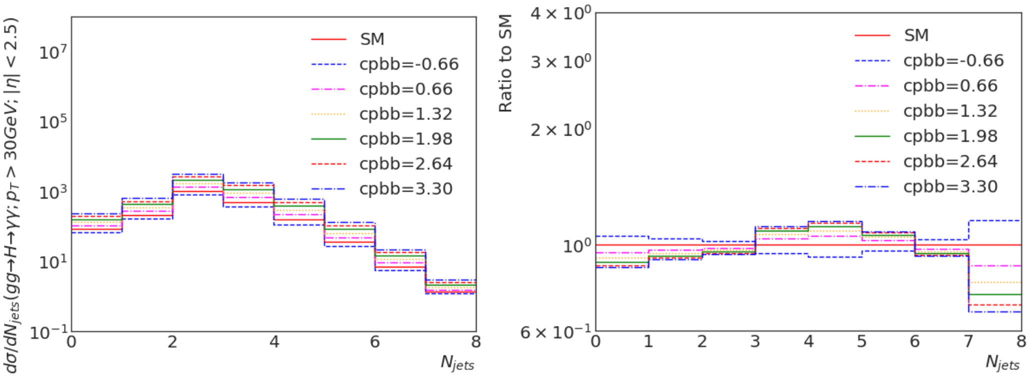

Figure 3.27: SM (red, solid) and cpbb operator coefficient value contributions for N_{jets}. The right panel gives the normalized ratio with respect to the SM prediction

Chapter 4

Summary

We have presented the SMEFT formalism as a tool to probe new physics. In the SMEFT framework Beyond Standard Model (BSM) effects are parametrized through a class of higher-dimensional operators. The operators which are relevant for the Higgs Physics are dimension-six operators. In this master thesis, we have performed a phenomenological study of the possible effects of dimension-six operators, by looking into the effect of the variations of operator coefficients cpg,ctp, ctg, cpbb on Higgs observables. Variation of the coefficients is done concerning the requirement that the cross-section remains below 10% of statistical precision. Interpretation of the impact that SMEFT operators have on the observables is based on the chi-square metric.

We have interpreted the results following two main steps. First, we looked at the same operator coefficient value and different observables. Followed by same observable but different operator coefficients keeping their value fixed for all operator coefficients we choose to interpret. The results of this master thesis can be summarized as follows:

Variations of different SMEFT operators affect the observables spectrum in different regions. Direct coupling of Higgs with gluons($\mathcal{O}_1$) affects the spectrum mostly on high energies of the observable tail. Besides, negative variation tends to harden the spectrum more than positive values. Modification of the Higgs-top Yukawa ($\mathcal{O}_2$) affects mostly the normalization and simply rescales the spectrum for the relevant observables. A chromomagnetic operator ($\mathcal{O}_3$) according to our metric results to be the coefficient operator which has shown the lowest impact for ctg=-0.2 among all observables and operators, resulting in the lowest chi-square value for the transverse momentum spectrum of jet (p_T^{jet}) observable. CP conserving operator relevant for the Higgs decay ($\mathcal{O}_4$) it is not sensitive for the same value variations as for cpg, ctp, ctg. However, for a given value the biggest impact it is shown in high observable tail coming from positive variation values. The observable which is most sensitive for this operator coefficient it is transverse momentum spectrum of the diphoton pair.

On the whole, the biggest impact on observables is coming from positive values of the operator coefficients, especially from the direct coupling of Higgs with gluons. The biggest impact among all observables and coefficients in our work it is coming from the positive value of cpg =1.0 contributions on transverse momentum spectrum of the diphoton pair $p_T^{\gamma\gamma}$.

Concerning the different coefficients for a fixed variation value and the same observable. We started the comparison of cpg, ctp, ctg = -0.2, where the ctp has the biggest impact on all observables, leading with a number of jets for $\eta < 2.5$ variable as the most sensitive one because of the largest chi-square value. For ctp, ctg = -1.0, direct coupling of Higgs with gluons dominates with a bigger impact on observables compared to modification of the top Yukawa, leading with the observable for the transverse momentum spectrum of the diphoton pair. Regarding the various values of ctg, cpg for 0.2 and 1.0 direct coupling of the Higgs has a bigger impact on observables compared to the ctg contributions on differential cross-section distributions.

Appendix A

Differential distributions for $|\eta| < 4.7$

Here we present the differential distributions coming from the impact of the operator coefficients on the observables:

p_T^{jet} - transverse momentum spectrum of the jet, considering only jets with $|\eta| < 4.7$.

N_{jets} - number of jets in the event with $|\eta| < 4.7$ and $p_T > 30GeV$.

From Figure A.1 to A.10 the SM and operator coefficient values contributions for p_T^{jet} and N_{jets} are displayed. Table A.1 shows us the impact of the operator coefficients on the number of jets and transverse momentum spectrum of jet, based on χ^2 values. These numbers tell us which observable is more sensitive to a given value of the coefficient.

For positive (negative) values of cpg=1.0 (cpg=-1.0) the observable for the transverse momentum of the jet (p_T^{jet}) is more sensitive (see Fig.A.1 and A.2) than number of jets observable N_{jets} (see Fig.A.3 and A.4). These observables turn out to be more sensitive for this variation value because give higher chi-square value compared to cpg=0.2 (cpg=-0.2). Overall, the observable p_T^{jet} is the most sensitive one, by giving the largest χ^2 value for cpg=1.0 from all the operator coefficients presented in Table A.1.

For the modification of the top Yukawa operator coefficient, observables are more sensitive to ctp=-0.2 value rather than ctp=-1.0. The most sensitive observable is the number of jets N_{jets} (see FigA.6) which gives larger chi-square value compared to the transverse momentum spectrum of jet.

Regarding the contribution of the chromomagnetic operator coefficient on the observables, positive values have a bigger impact than negative ones. For ctg=1.0 the observable N_{jets} (see Fig.A.8) is more sensitive to this given value of the coefficient because have larger chi-square than transverse momentum spectrum of the jet (Fig.A.7).

The impact of the cpbb operator coefficient on the number of jets and transverse momentum spectrum of a jet is visible in Table A.1. The observable for the number of jets tend to be more sensitive for cpbb=3.30 (Fig.A.10) compared to the transverse momentum spectrum of a jet. Overall, negative variations of the coefficients tend to have less impact on the variable than positive ones.

When we check for different operator coefficients for fixed values and same observables then this follows:

For cpg,ctp,ctg=-0.2, the largest chi-square value is coming from modification of the top Yukawa coefficient (ctp) (see Fig.A.5 and A.6) followed by cpg and ending with ctg coefficient contribution. This signature leads with transverse momentum spectrum of jet (p_T^{jet}), which is more sensitive than number of jets variable (N_{jets}) for this fixed value of the variation.

For cpg, ctg = 0.2 larger chi-square is coming from the direct coupling of Higgs with gluons operator coefficient, which means bigger the impact on observables of the transverse momentum of jet and number of jets compared to chromomagnetic operator coefficient (ctg) (see Fig.A.2 and A.4). This holds also for cpg, ctg = 1.0.

In addition, for cpg, ctp = -1.0 , direct coupling of Higgs with gluons coefficient dominates for this given value, because it shows larger chi-square value than ctp for the observable p_T^{jet} and N_{jets} (see Fig.A.1 and A.3).

Observable	Coefficient values	χ^2 values
p_T^{jet}	cpg=-1.0	194865213
	cpg=-0.2	21774
	cpg=1.0	331657150
	cpg=0.2	583202
N_{jets}	cpg=-1.0	185438249
	cpg=-0.2	13114
	cpg=1.0	317438052
	cpg=0.2	536279
p_T^{jet}	ctp=-1.0	98635
	ctp=-0.2	109949
N_{jets}	ctp=-1.0	98736
	ctp=-0.2	110051
p_T^{jet}	ctg=1.0	143408
	ctg=-0.2	2515
	ctg=0.2	3443
N_{jets}	ctg=1.0	144304
	ctg=-0.2	2528
	ctg=0.2	3462
p_T^{jet}	cpbb=-0.66	6429
	cppb=0.66	10987
	cppb=3.30	593710
N_{jets}	cpbb=-0.66	6475
	cpbb=0.66	11075
	cppb=3.30	598889

Table A.1: Impact of the operator coefficients cpg, ctg, ctp, cpbb on observables based on χ^2 values.

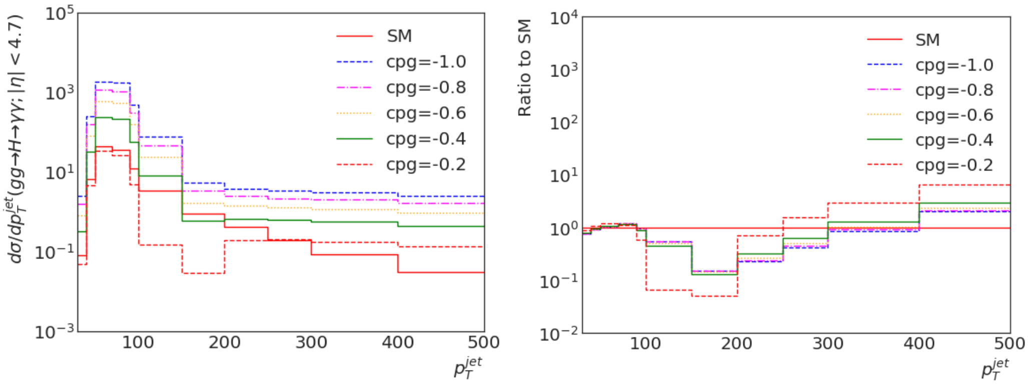

Figure A.1: SM (red, solid) and negative cpg operator coefficient value contributions for p_T^{jet}. The right panel gives the normalized ratio with respect to the SM prediction

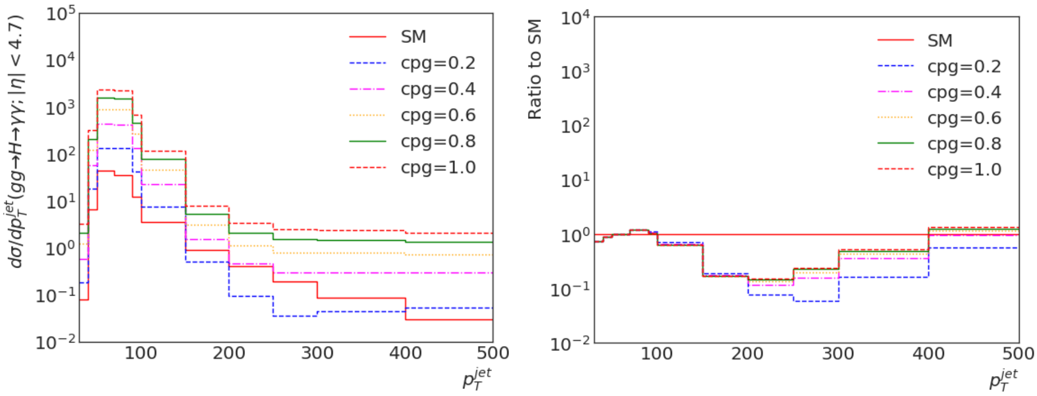

Figure A.2: SM (red, solid) and positive cpg operator coefficient value contributions for p_T^{jet}. The right panel gives the normalized ratio with respect to the SM prediction

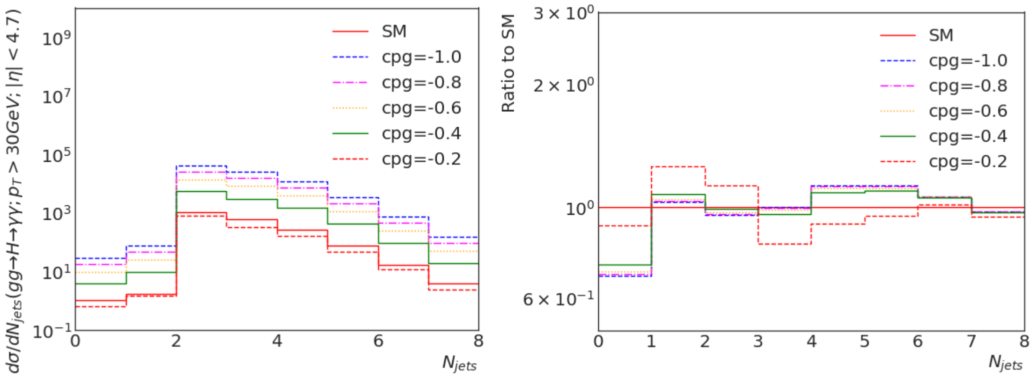

Figure A.3: SM (red, solid) and negative cpg operator coefficient value contributions for N_{jets}. The right panel gives the normalized ratio with respect to the SM prediction

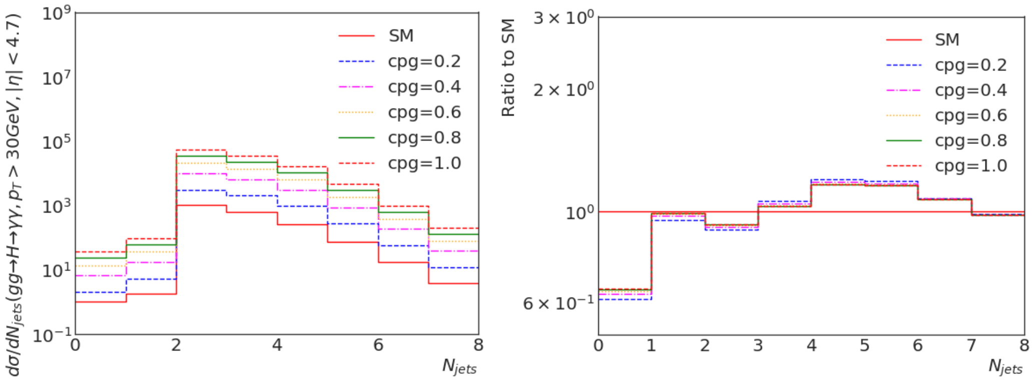

Figure A.4: SM (red, solid) and positive cpg operator coefficient value contributions for N_{jets}. The right panel gives the normalized ratio with respect to the SM prediction

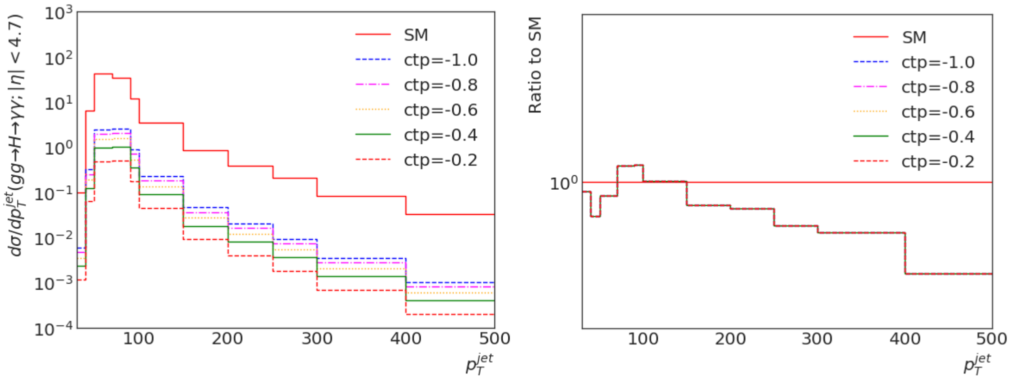

Figure A.5: SM (red, solid) and negative ctp operator coefficient value contributions for p_T^{jet}. The right panel gives the normalized ratio with respect to the SM prediction

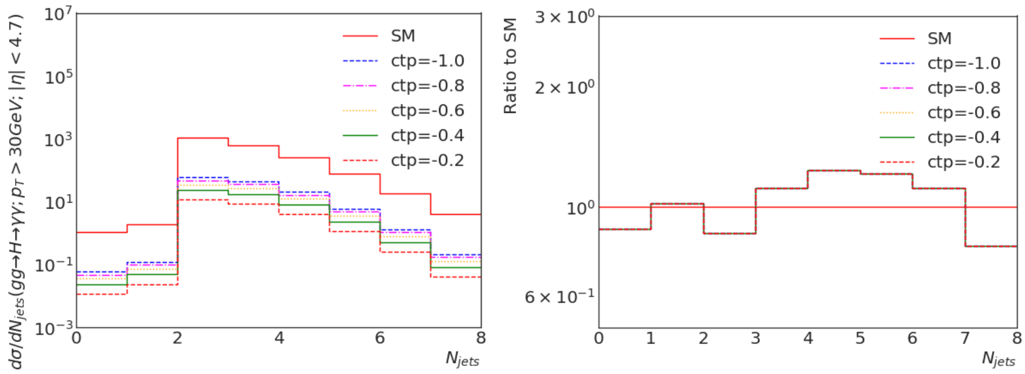

Figure A.6: SM (red, solid) and negative ctp operator coefficient value contributions for N_{jets}. The right panel gives the normalized ratio with respect to the SM prediction

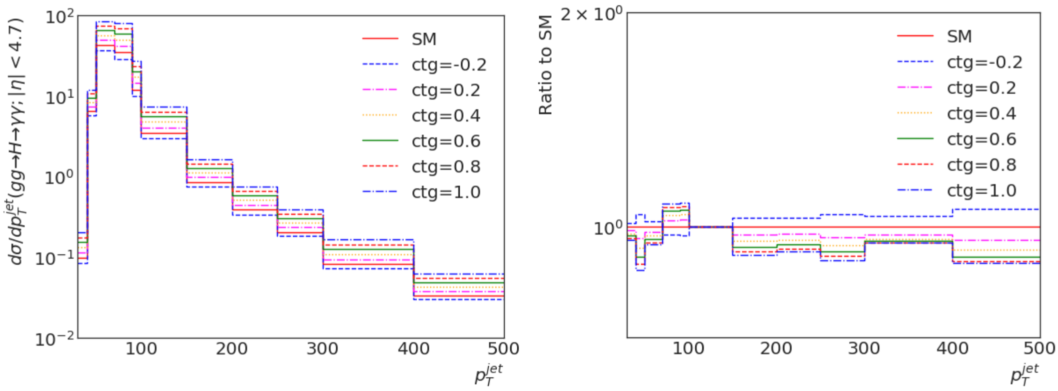

Figure A.7: SM (red, solid) and ctg operator coefficient value contributions for p_T^{jet}. The right panel gives the normalized ratio with respect to the SM prediction

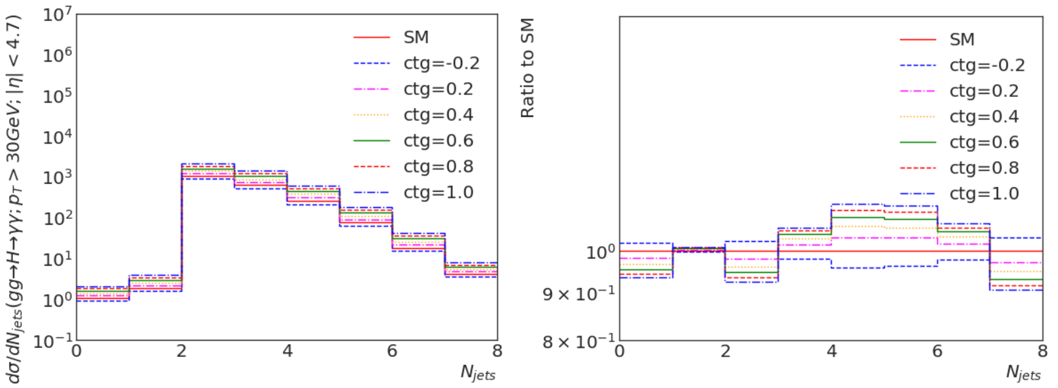

Figure A.8: SM (red, solid) and ctg operator coefficient value contributions for N_{jets}. The right panel gives the normalized ratio with respect to the SM prediction

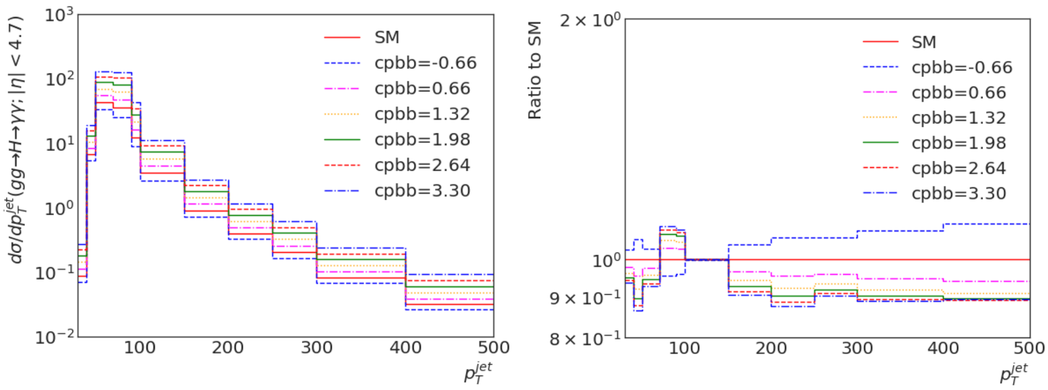

Figure A.9: SM (red, solid) and cpbb operator coefficient value contributions for p_T^{jet}. The right panel gives the normalized ratio with respect to the SM prediction

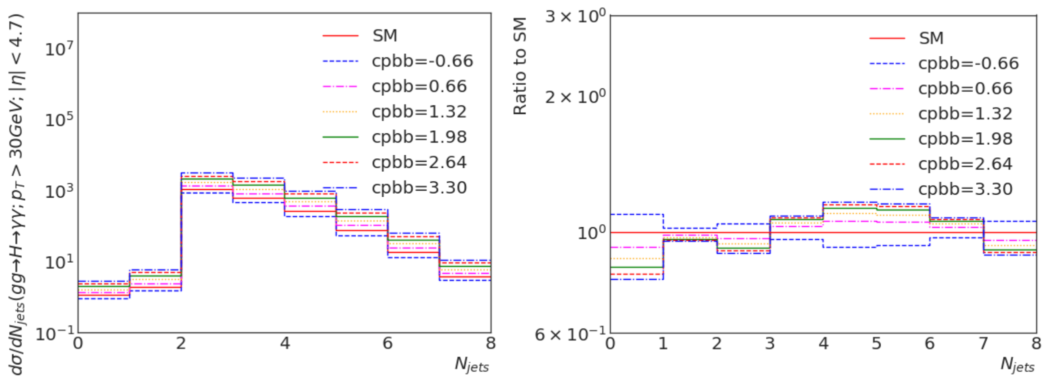

Figure A.10: SM (red, solid) and cpbb operator coefficient value contributions for N_{jets}. The right panel gives the normalized ratio with respect to the SM prediction

Appendix B

Differential distributions for Higgs rapidity

Here we present the differential distributions coming from the impact of the operator coefficients on the observables:

$\eta^{\gamma\gamma}$ - the rapidity spectrum of the diphoton pair.

η^{γ_1} - the rapidity spectrum of the first photon.

η^{γ_2} - the rapidity spectrum of the second photon.

From Figures B.1 to B.15 the SM and operator coefficient values contributions for rapidity distributions are displayed. Table B.1 shows us the impact of the operator coefficients on $\eta^{\gamma\gamma}$, η^{γ_1} and η^{γ_2} based on χ^2 values. These numbers tell us which observable is more sensitive to a given value of the coefficient. Based on the work done in [34] the dimension-six operators have no impact on the shape of the rapidity distribution, however, we present them as the part of the work.

First, comparing the chi-square values we see that observables are mostly affected by positive value variations because chi-square values are higher for cpg=1.0, 0.2 than for cpg = -1.0, -0.2. The most sensitive observable among all operator coefficient variations turns out to be rapidity spectrum of the first photon η^{γ_1} (see Fig.B.4) for cpg=1.0, followed by negative value of cpg = -1.0 for η^{γ_1} (see Fig.B.3). Predominantly, positive values of operator coefficients give larger chi-square values than negative ones, which makes the rapidity observables more sensitive for positive values of the cpg.

From Table B.1 we can see the impact of the ctp values on rapidity observables. If we compare chi-square values for ctp we see that biggest impact is coming from ctp = -0.2 rather than ctp=-1.0 (see Fig.B.7, B.9, B.11). However, the chi-square values are very similar. For example, the chi-square values for rapidity of the first and second photon (η^{γ_1}, η^{γ_2}) for ctp = -0.2 are similar.

Regarding to the contribution of the chromomagnetic operator coefficient (see Fig.B.8, B.10, B.12), the observable with the highest chi-square value for ctg=1.0 is rapidity spectrum for the first photon (η^{γ_1}) present on Fig.B.10. In addition, the chi-square values are very close to each other for $\eta^{\gamma\gamma}$ and η^{γ_2}. All in all, rapidity distributions are more sensitive for positive value variations than for negative ones (see Table B.1).

For cpbb, the sensitivity is not present for the same value variations like for cpg, ctp, ctg. However, we have shown some values which give chi-square values different from zero. From the Table B.1 we can see cpbb=3.30 has the biggest impact on η^{γ_1} observable (see Fig.B.14). Besides, larger chi-square number for the positive value of cpbb tell us that the rapidity differential cross-section distribution are more sensitive to these values rather than for negative values of the operator coefficients.

When we check for different operator coefficient for a fixed value and same observable we can find which operator coefficient affects rapidity observables the most.

For cpg,ctp,ctg=-0.2, the largest chi-square value is coming from modification of the top Yukawa coefficient (ctp) followed by cpg and ending with ctg coefficient contribution. This signature leads with rapidity spectrum of η^{γ_2} or η^{γ_1} (see Fig.B.9 and B.11), which are more sensitive than rapidity spectrum of diphoton pair $\eta^{\gamma\gamma}$ (see Fig.B.7) for this fixed value of the variation.

For cpg, ctg = 0.2 larger chi-square is coming from direct coupling of Higgs with gluons operator coefficient, which means bigger the impact on rapidity observables compared to chromomagnetic operator coefficient (ctg) (see Fig.B.2, B.4, B.6). This holds also for cpg, ctg = 1.0.

Also, for cpg, ctp = -1.0, direct coupling of Higgs with gluons coefficient dominates for this given value, because it shows larger chi-square value than ctp for the observables. Leading with rapidity spectrum for the first photon (see Fig.B.3) and followed by rapidity spectrum for the second photon (see Fig.B.5) and the last sensitive one rapidity spectrum of the diphoton pair (see Fig.B.1).

Observable	Coefficient values	χ^2 values
$\eta^{\gamma\gamma}$	cpg=-1.0	181222418.
	cpg=-0.2	13061.
	cpg=1.0	309820893.
	cpg=0.2	523169.
η^{γ_1}	cpg=-1.0	185163518.
	cpg=-0.2	12382.
	cpg=1.0	315899610.
	cpg=0.2	524761.
η^{γ_2}	cpg=-1.0	185133903.
	cpg=-0.2	12323.
	cpg=1.0	315869275.
	cpg=0.2	524709.
$\eta^{\gamma\gamma}$	ctp=-1.0	94201.
	ctp=-0.2	105239.
η^{γ_1}	ctp=-1.0	98722.
	ctp=-0.2	110059.
η^{γ_2}	ctp=-1.0	98723.
	ctp=-0.2	110059.
$\eta^{\gamma\gamma}$	ctg=1.0	141050.
	ctg=-0.2	2471.
	ctg=0.2	3385.
η^{γ_1}	ctg=1.0	141359.
	ctg=-0.2	2477.
	ctg=0.2	3392.
η^{γ_2}	ctg=1.0	141348.
	ctg=-0.2	2477.
	ctg=0.2	3392.
$\eta^{\gamma\gamma}$	cpbb=-0.66	6324.
	cpbb=0.66	10815.
	cpbb=3.30	584763.
η^{γ_1}	cpbb=-0.66	6342.
	cpbb=0.66	10844.
	cpbb=3.30	586295.
η^{γ_2}	cpbb=-0.66	6339.
	cpbb=0.66	10840.
	cpbb=3.30	586065.

Table B.1: Impact of the operator coefficients cpg, ctg, ctp, cpbb on observables based on χ^2 values.

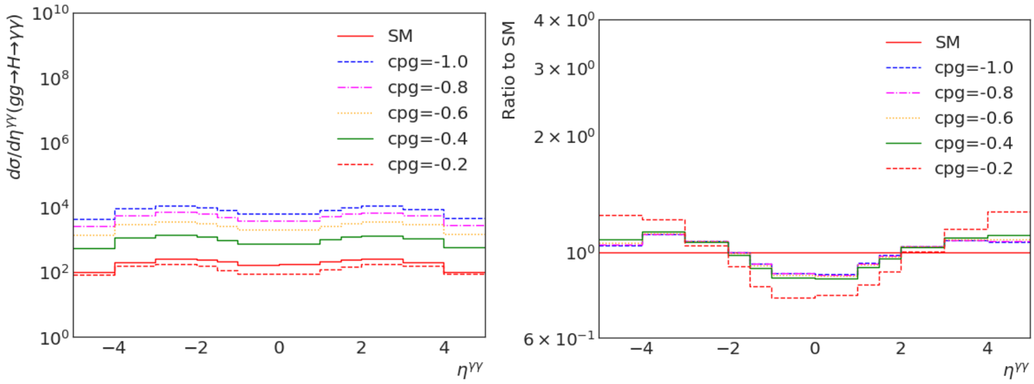

Figure B.1: SM (red, solid) and negative cpg operator coefficient value contributions for $\eta^{\gamma\gamma}$. The right panel gives the normalized ratio with respect to the SM prediction

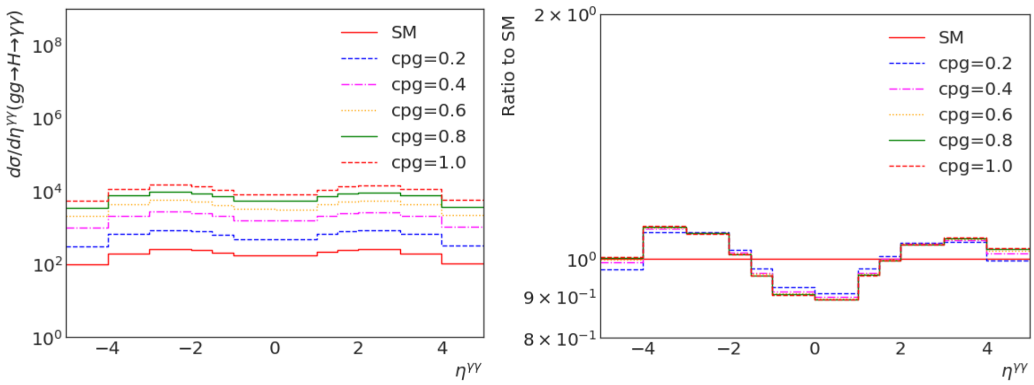

Figure B.2: SM (red, solid) and positive cpg operator coefficient value contributions for $\eta^{\gamma\gamma}$. The right panel gives the normalized ratio with respect to the SM prediction

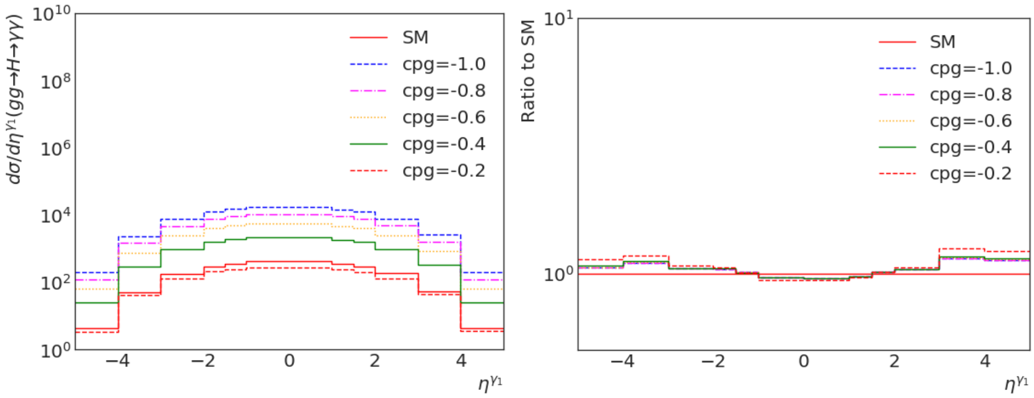

Figure B.3: SM (red, solid) and negative cpg operator coefficient value contributions for η^{γ_1}. The right panel gives the normalized ratio with respect to the SM prediction

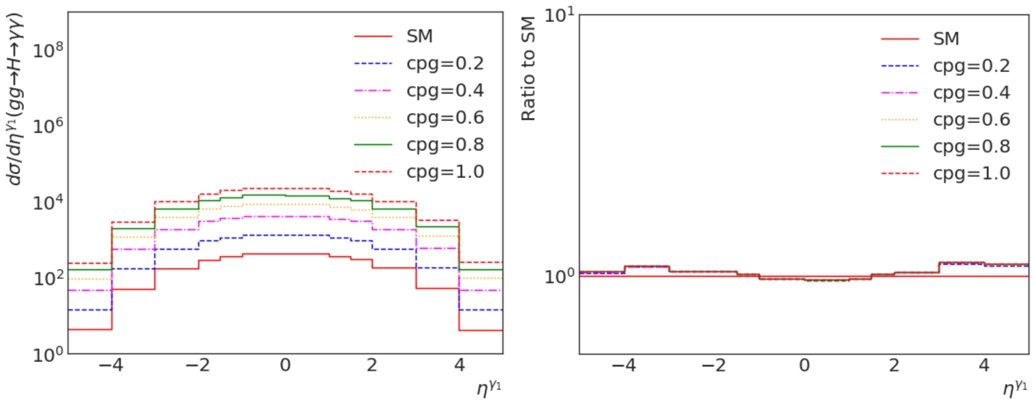

Figure B.4: SM (red, solid) and positive cpg operator coefficient value contributions for η^{γ_1}. The right panel gives the normalized ratio with respect to the SM prediction

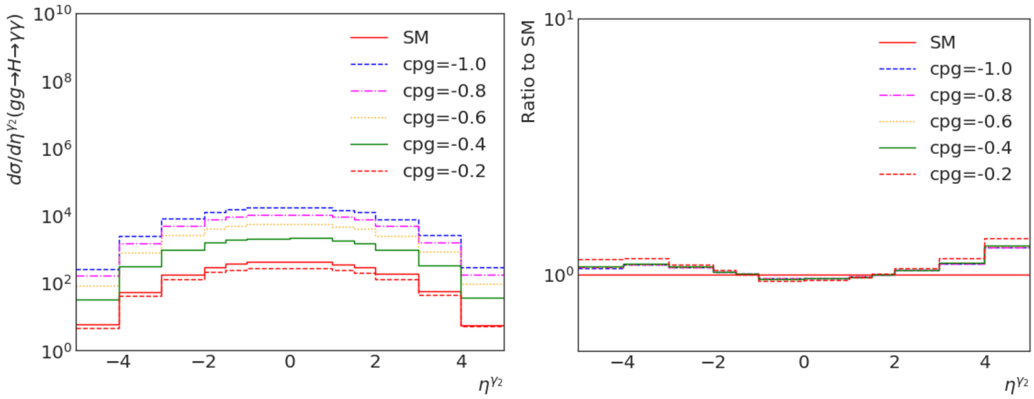

Figure B.5: SM (red, solid) and negative cpg operator coefficient value contributions for η^{γ_2}. The right panel gives the normalized ratio with respect to the SM prediction

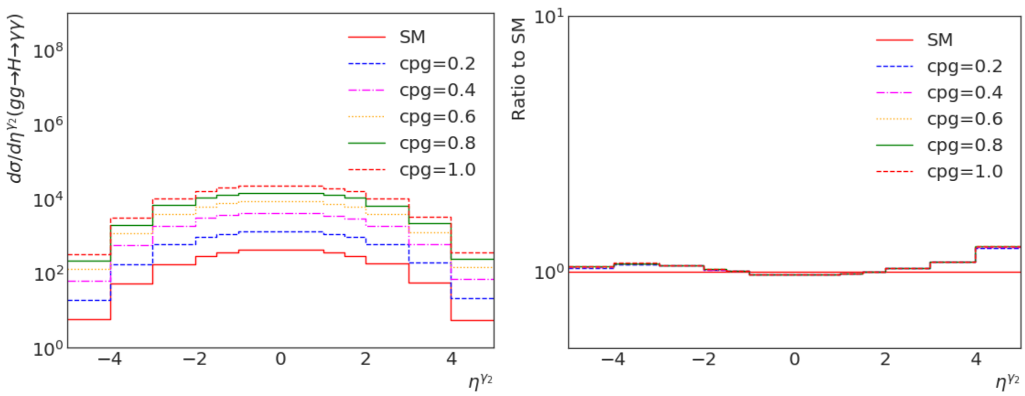

Figure B.6: SM (red, solid) and positive cpg operator coefficient value contributions for η^{γ_2}. The right panel gives the normalized ratio with respect to the SM prediction

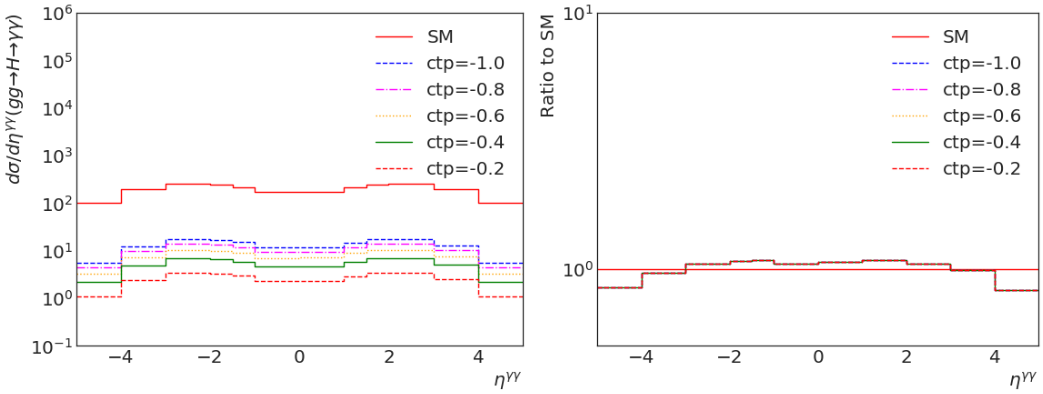

Figure B.7: SM (red, solid) and negative ctp operator coefficient value contributions for $\eta^{\gamma\gamma}$.The right panel gives the normalized ratio with respect to the SM prediction

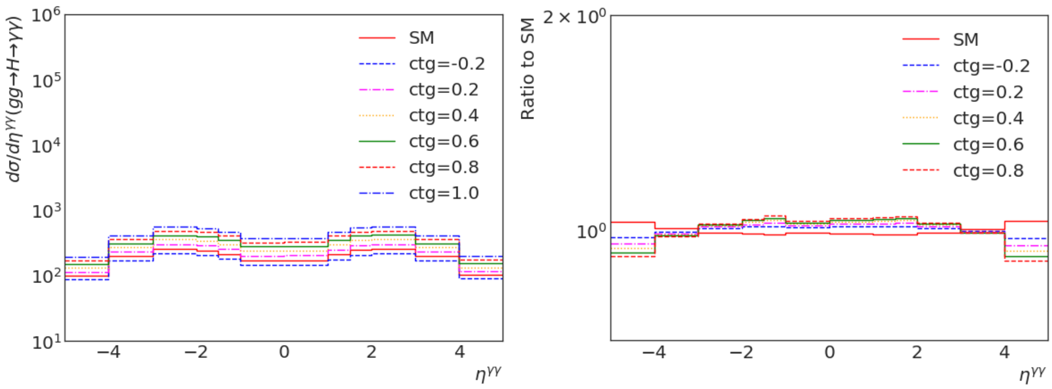

Figure B.8: SM (red, solid) and ctg operator coefficient value contributions for $\eta^{\gamma\gamma}$. The right panel gives the normalized ratio with respect to the SM prediction

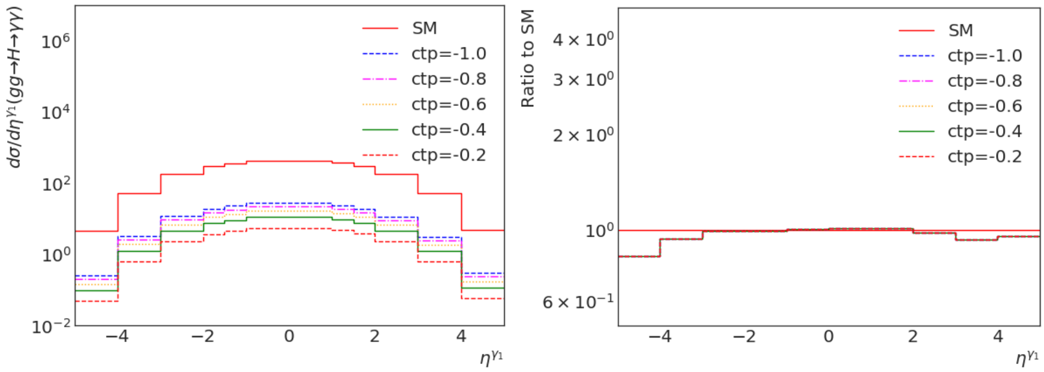

Figure B.9: SM (red, solid) and negative ctp operator coefficient value contributions for η^{γ_1}. The right panel gives the normalized ratio with respect to the SM prediction

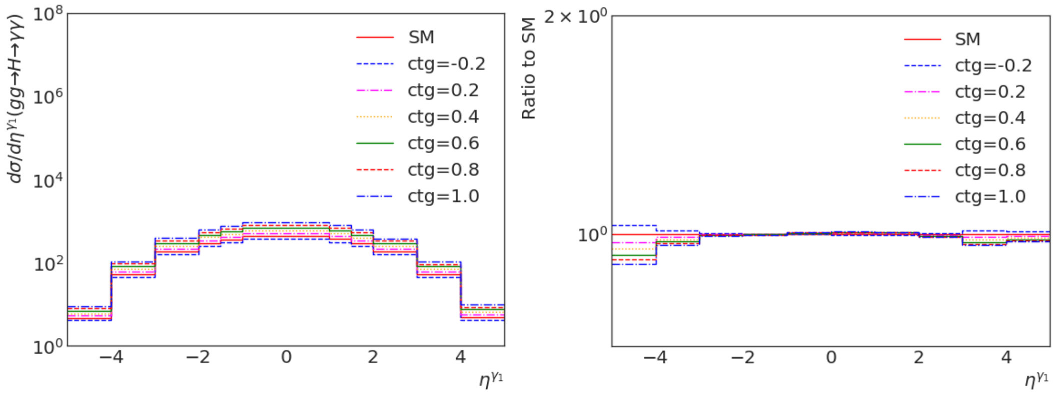

Figure B.10: SM (red, solid) and ctg operator coefficient value contributions for η^{γ_1}. The right panel gives the normalized ratio with respect to the SM prediction

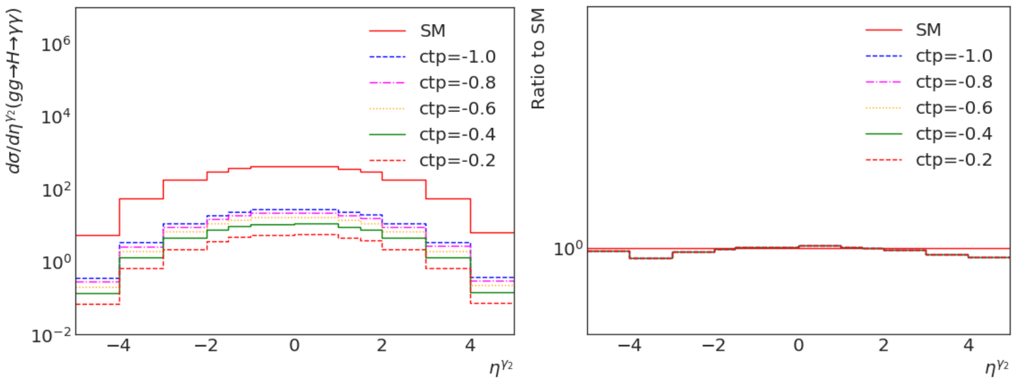

Figure B.11: SM (red, solid) and negative ctp operator coefficient value contributions for η^{γ_2}. The right panel gives the normalized ratio with respect to the SM prediction

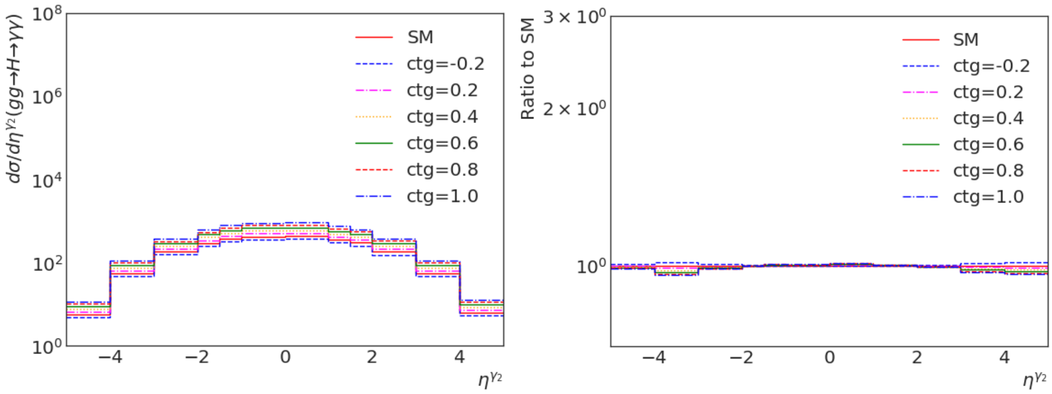

Figure B.12: SM (red, solid) and ctg operator coefficient value contributions for η^{γ_2}. The right panel gives the normalized ratio with respect to the SM prediction

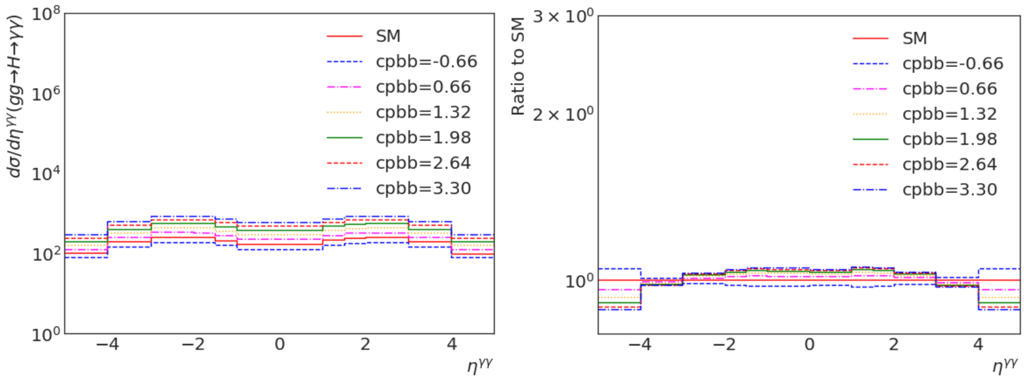

Figure B.13: SM (red, solid) and cpbb operator coefficient value contributions for $\eta^{\gamma\gamma}$. The right panel gives the normalized ratio with respect to the SM prediction

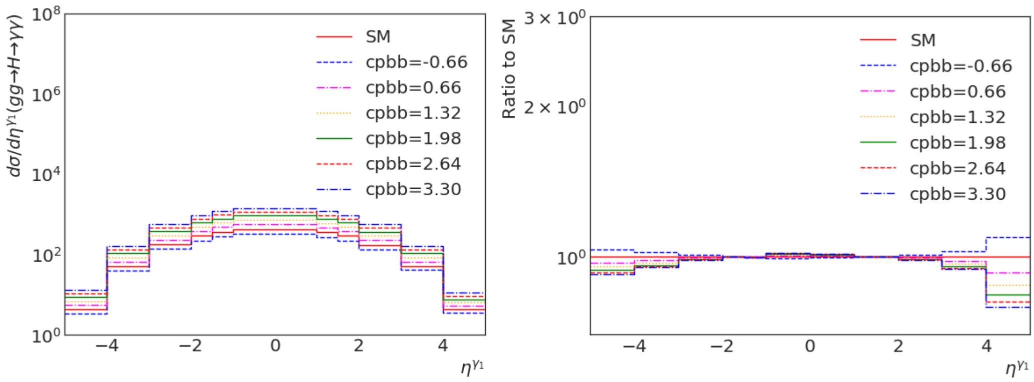

Figure B.14: SM (red, solid) and cpbb operator coefficient value contributions for η^{γ_1}. The right panel gives the normalized ratio with respect to the SM prediction

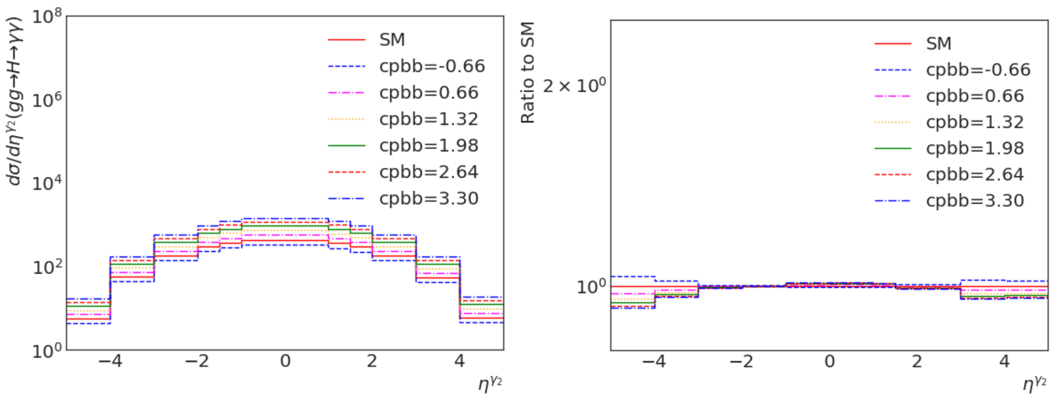

Figure B.15: SM (red, solid) and cpbb operator coefficient value contributions for η^{γ_2}. The right panel gives the normalized ratio with respect to the SM prediction

Bibliography

[1] An Introduction to PYTHIA 8.2. *Comput. Phys. Commun*, 191:159–177, 2015.

[2] M. Spira A. Djouadi and P. M. Zerwas. Production of Higgs boson in proton collider: QCD corrections. *Phys. Lett*, B264:440–446, (1991).

[3] David Grellscheid Hendrik Hoeth Leif Lonnblad James Monk Holger Schulz Frank Siegert Andy Buckley, Jonathan Butterworth. Rivet user manual. *JHEP*, (28 Feb.2013).

[4] The ATLAS and CMS Collaborations. Measurements of the Higgs boson production and decay rates and constraints on its couplings from a combined ATLAS and CMS analysis of the LHC pp collision data at $\sqrt{s} = \mathbf{7}$ and 8 TeV. *JHEP08(2016)045*.

[5] M. Misiak B. Grzadkowski, M. Iskrzynski and J. Rosiek. Dimension-Six Terms in the Standard Model Lagrangian. *JHEP 1010*, 085, 2010.

[6] John N. Bahcall. Solar Neutrinos. I. Theoretical. *Phys.Rev.Lett*, 12:300, (1964).

[7] Ilaria Brivio and Michael Trott. The Standard Model as an Effective Field Theory. *Phys.Lett.*, Volume 793:1–168, 12 Nov. 2018.

[8] S. Bucherer A. Daleo Z.Kunszt C. Anastasiou, S. Beerli. Two-loop amplitudes and master integrals for the production of a Higgs boson via a massive quark and a scalar-quark loop. *JHEP01*, 2007, (23.01.2007).

[9] C.Anastasiou and K.Melnikov. Higgs boson production at hadron colliders in NNLO QCD. *Nuck.Phys*, B646:220–256, (2002).

[10] F.Dulat E. Furlan T. Gehrmann F. Herzog A. Lazopoulos C.Anastasiou, C.Duhr and B. Mistlberger. High precision determination of the gluon fusion Higgs boson cross-section at LHC. *JHEP*, 05:058, (2016).

[11] S.Bucherer C.Anastasiou and HPro: Z.Kunszt. A NLO Monte-Carlo for Higgs production via gluon fusion with finite heavy quark masses,. *JHEP*, 10:068, (2009).

[12] Planck collaboration. *Astronomy Astrophysics*, 594,A13:63, 2016.

[13] S. Dawson. Radiative corrections to Higgs boson production. *Nucl.Phys*, B359:283–300, (1991).

[14] S. Dawson and R. Kauffman. QCD corrections to Higgs boson production:nonleading terms in the heavy quark limit. *Phys.Rev*, D49:2298–2309, (1994).

[15] M.Spira D.Graudenz and A.Djouadi P. M. Zerwas. Higgs boson production at the LHC. *Nucl.Phys.*, B453:17–82, (1995).

[16] M.Spira D.Graudenz and P. M. Zerwas. QCD corrections to Higgs boson production at proton proton colliders. *Phys. Rev.Lett*, 70:1370–1375, (1993).

[17] Georges Aad et al. Observation of a new partice in the search for the Standard Model Higgs Boson with ATLAS detector at the LHC. *Phys.Lett.*, B716:1-29, 2013.

[18] Sergeuei Chatrchyan et al. Observation of a new boson at a mass of 125 GeV with the CMS experiment at the LHC. *Phys.Lett.*, B716:30-61, 2013.

[19] Adam Falkowski. Effective field theory approach to LHC Higgs data. *Pramana*, 87, 2016.

[20] F.Zwicky. The redshift of extragalactic nebulae. *Helvetica Physica Acta, Vol. 6, p. 110-127*, (1933).

[21] Cecilia E. Gerber. LHC Highlights and Prospects. *JHEP*, (24.09.2019).

[22] Jenkins E.E. Manohar A. V. Grojean, C. and M.(2013) Trott. Renormalization Group Scaling of Higgs Operators and $\Gamma(h \longrightarrow \gamma\gamma)$. *JHEP*, 04, 016.

[23] R. V. Harlander and W. B. Kilgore. Next-to-next-to-leading order Higgs production at hadron colliders. *Phys.Rev.Lett*, 88:201801, (2002).

[24] Christine Hartmann and Michael Trott. Higgs Decay to Two Photons at One Loop in the Standard Model Effective Field Theory. *Phys.Rev.Lett.*, 115,191801, (06.11.2015).

[25] S. Frixione V. Hirschi F. Maltoni O. Mattelaer H.-S. Shao T. Stelzer P. Torrielli M. Zaro J. Alwall, R. Frederix. The automated computation of tree-level and next-to-leading order differential cross sections, and their matching to parton shower simulations. *JHEP*, 079, (21.07.2014).

[26] S. Glaus M. M. Muhlleitner J. Ronca M. Spira-J. Streicher J. Baglio, F. Campanario. Higgs-pair production via gluon fusion at hadron colliders: NLO QCD corrections. *JHEP04*, (2020).

[27] G.Hulth L.Bergström. Induced Higgs Couplings to Neutral Bosons in e^+e^- Collisions. *Nuclear Physics*, B259:137–155, (1985).

[28] S. Jahn Stephen P. Jones M.Kerner J.Schlenk H.Yokoya L.Chen, G.Heinrich. Photon pair production in gluon fusion: Top quark effects at NLO with threshold matching. *JHEP*, 115, (21.11.2019).

[29] M. Spira M. Grazzini, A.Ilnicka and M. Wiesemann. Modeling BSM effects on the Higgs transverse-momentum spectrum in an EFT approach. *JHEP 03*, 115, 2017.

[30] M.Spira M. Grazzini, A. Ilnicka. Higgs boson production at large transverse momentum within SMEFT: analytical results. *The European Physical Journal C*, 78, 808(2018).

[31] H. M. Georgi S. L. Glashow M. E. Machacek and D. v.Nanopoulos. Higgs Bosons from Two Gluon Annihilation in Proton Proton Collisions. *Phys.Rev.Lett 40,692*, (1978).

[32] A. V. Manohar and M.B.(2006) Wise. Modifications to the properties of the Higgs boson. *Phys. Lett*, B636:107–113.

[33] Aneesh V. Manohar. Introduction to Effective Field Theories. *JHEP*, pages 74–81.

[34] F. Maltoni E.Vryonidou N. Deutschmann, C.Duhr. Gluon-fusion Higgs production in the Standard Model Effective Field Theory. *JHEP*, 63, (9 March 2018).

[35] SNO Collaboration Q. R. Ahmad. Measurement of the rate of $\nu_e + d \longrightarrow p + p + e^-$ interactions produced by 8B solar neutrinos at the Sudbury Neutrino Observatory. *Phys.Rev.Lett.*, 87:071301, (2001).

[36] SNO Collaboration Q. R. Ahmad. Direct Evidence for Neutrino Flavor Transformation from Neutral-Current Interactions in the Sudbury Neutrino Observatory. *Phys.Rev.Lett.*, 89:011301, (2002).

[37] A. V. Manohar M.Trott R. Alonso, E.E. Jenkins. Renormalization Group Evolution of the Standard Model Dimension Six Operators III: Gauge Coupling Dependence and Phenomenology. *JHEP*, 1404:159, (2014).

[38] Jr. Raymond Davis. Solar Neutrinos. II. Experimental. *Phys.Rev.Lett*, 12:303, (1964).

[39] R.Harlander and P.Kant. Higgs production and decay: Analytic results at next-to-leading order QCD. *JHEP*, 12:015, (2005).

[40] W. Kent Jr. Rubin, Vera C.; Ford. Rotation of the Andromeda Nebula from a Spectroscopic Survey of Emission Regions. *Astrophysical Journal*, 159:P.379, February 1970.

[41] Matthew D. Schwartz. *QUANTUM FIELD THEORY and the STANDARD MODEL*. Cambridge University Press, 2014.

[42] S.Frixione and B. R. Webber. Matching NLO QCD computations and parton shower simulations. *JHEP*, 06:029, (2002).

[43] Y. Fukuda et al The Super-Kamiokande Collaboration. Evidence for oscillation of atmospheric neutrinos. *Phys.Rev.Lett.*, 81:1562, (24 August 1998).

[44] J.Smith V. Ravindran and W.L.van Neerven. NNLO corrections to the total cross section for Higgs boson production in hadron hadron collisions. *Nucl.Phys*, B665:325–366, (2003).

[45] M.E.Shaposhnikov V.A.Kuzmin, V.A.Rubakov. On anomalous electroweak baryon-number non-conservation in the early universe. *Phys.Lett.*, 155B:Pages 36–42, (16 May 1985).

[46] D. Wyler W. Buchmuller. Effective Lagrangian Analysis of New Interactions and Flavor Conservation. *Nucl.Phys.*, B268, (1986).

ETH

Eidgenössische Technische Hochschule Zürich
Swiss Federal Institute of Technology Zurich

Declaration of originality

The signed declaration of originality is a component of every semester paper, Bachelor's thesis, Master's thesis and any other degree paper undertaken during the course of studies, including the respective electronic versions.

Lecturers may also require a declaration of originality for other written papers compiled for their courses.

I hereby confirm that I am the sole author of the written work here enclosed and that I have compiled it in my own words. Parts excepted are corrections of form and content by the supervisor.

Title of work (in block letters):

Study of SMEFT BSM operators in the context of the CMS $H \rightarrow \gamma\gamma$ analysis using NLO simulation

Authored by (in block letters):
For papers written by groups the names of all authors are required.

Name(s):	**First name(s):**
QUNI	BARDH

With my signature I confirm that
- I have committed none of the forms of plagiarism described in the '<u>Citation etiquette</u>' information sheet.
- I have documented all methods, data and processes truthfully.
- I have not manipulated any data.
- I have mentioned all persons who were significant facilitators of the work.

I am aware that the work may be screened electronically for plagiarism.

Place, date	**Signature(s)**
ZURICH, September 10th, 2020	BQuni

For papers written by groups the names of all authors are required. Their signatures collectively guarantee the entire content of the written paper.